Economic Geology, v. 117, no. 5, pp. 1043–1071

Pluton Exhumation in the Precordillera of Northern Chile (17.8°–24.2°S): Implications for the Formation, Enrichment, and Preservation of Porphyry Copper Deposits

Simon I.R. Dahlström,[1,†] Frances J. Cooper,[1] Jon Blundy,[2] Simon Tapster,[3] Jaime Cortés Yáñez,[4] and Laura A. Evenstar[5]

[1]*School of Earth Sciences, University of Bristol, Bristol BS8 1RJ, UK*

[2]*Department of Earth Sciences, University of Oxford, Oxford OX1 3AN, UK*

[3]*Geochronology and Tracers Facility, British Geological Survey, Nottingham NG12 5GG, UK*

[4]*BHP Metals Exploration, Tucson, Arizona 85704, USA*

[5]*School of Applied Sciences, University of Brighton, Brighton BN2 4GJ, UK*

Abstract

Hypogene mineralization in porphyry Cu deposits is typically associated with crustal thickening and rapid exhumation, whereas supergene enrichment requires slow exhumation to allow sufficient time for leaching and downward transport of Cu before it is lost to surface erosion. Therefore, spatial and temporal patterns of exhumation within a metallogenic belt can highlight favorable locations for hypogene mineralization, supergene enrichment, and preservation. Here, we determine average pluton exhumation rates along an ~730-km segment of the middle Eocene-early Oligocene metallogenic belt in northern Chile (17.8°–24.2°S). By combining zircon U-Pb geochronology with Al-in-hornblende geobarometry, we pinpoint the time and depth at which each pluton was emplaced and use the age of overlying cover units or supergene minerals to date its arrival at the surface (or near-surface) environment.

Uranium-lead zircon ages for 49 samples from plutons and porphyries range from Carboniferous to Eocene (~314–35 Ma). Al-in-hornblende emplacement depths for 19 plutons are ~4–7 km, with one Carboniferous pluton emplaced at ~12 km. Two phases of net exhumation are identified: early Permian-Middle Triassic and middle Eocene-late Oligocene, with an intervening period of net burial. The highest exhumation rates (>0.30 km/m.y.) derive from the second phase, coeval with the Incaic orogeny and the main phase of hypogene mineralization. Present-day preservation of plutons and porphyry Cu deposits required low post-Oligocene average exhumation rates of <~0.01 km/m.y.—favorable for the development of many world-class supergene blankets. However, spatial variability in exhumation and burial across the belt led to poor conditions for supergene development locally: enrichment was hampered in some places by rapid exhumation after hypogene mineralization (e.g., ≥~4 km at El Abra), by burial beneath significant cover (e.g., Ministro Hales, Queen Elizabeth), or, in the Inti region of northernmost Chile, by a combination of the two.

Introduction

Porphyry copper deposits are the world's principal source of Cu and Mo (Sillitoe, 2010). The largest and highest-grade deposits commonly result from a two-stage process involving primary hypogene ore formation and secondary supergene enrichment, each favored by different geologic controls. During the hypogene stage, metal sulfides precipitate from magmatic-hydrothermal fluids to form an orebody, usually in the upper ~5 km of the crust (Seedorff et al., 2005; Wilkinson and Kesler, 2007; Singer et al., 2008; Yanites and Kesler, 2015). This is often associated with a compressional tectonic regime where crustal thickening and exhumation rates of several 100 m to over 1 km/m.y. prevail (Chivas et al., 1984; Kurtz et al., 1997; Sillitoe, 1998, 2010; Masterman et al., 2005; Yanites and Kesler, 2015; Sillitoe et al., 2019). Faster exhumation promotes efficient exsolution of metal-bearing fluids from magmas (Sillitoe, 1998; Cooke et al., 2005) and may facilitate telescoping, whereby early porphyry-style mineralization is overprinted and enriched by high-sulfidation mineralization at shallower crustal levels (Sillitoe, 1994, 1999; Masterman et al., 2005; Hervé et al., 2012; Maydagán et al., 2015; Sillitoe et al., 2019). Conversely, supergene enrichment occurs when hypogene ore sulfides, such as pyrite and chalcopyrite, are oxidized by meteoric water, and Cu is leached and transported in solution to the reducing conditions below the water table and reprecipitated in higher-grade sulfides such as chalcocite and covellite (Emmons, 1917; Sillitoe, 2005; Reich and Vasconcelos, 2015). In contrast to hypogene mineralization, this process requires slow exhumation that does not exceed the rate of downward Cu transport (Emmons, 1917; Brimhall et al., 1985; Hartley and Rice, 2005; Sillitoe, 2005; Riquelme et al., 2017; Sanchez et al., 2018). Supergene enrichment can more than triple the hypogene Cu grade (Sillitoe, 2005, 2010) and is often key to making a deposit economically viable. Constraining spatial and temporal patterns of exhumation during hypogene and supergene mineralization in porphyry Cu belts has potential as an exploration tool.

The Precordillera of northern Chile (Fig. 1A) hosts one of the most important porphyry Cu belts in the world, comprising middle Eocene-early Oligocene deposits, some of which have ore reserves exceeding 1 Gt (Sillitoe and Perelló, 2005). Several deposits exhibit both high hypogene Cu grades, often enhanced by late-stage high-sulfidation mineralization (Sillitoe and Perelló, 2005, and references therein),

†Corresponding author: e-mail, simon.dahlstrom@gmail.com

ISSN 0361-0128; doi:10.5382/econgeo.4912; 29 p.
Digital appendices are available in the online Supplements section.

Submitted: March 10, 2021 / Accepted: September 23, 2021

and world-class supergene enrichment zones (Sillitoe, 2005). These features suggest that exhumation rates were favorable for both hypogene and supergene mineralization, as well as for their subsequent preservation at near-surface levels. However, in northernmost Chile (north of ~19.5°S), there is scant evidence for porphyry Cu mineralization, perhaps due to extensive late Oligocene-early Miocene volcanic cover (e.g., García et al., 2017). The possibility of undiscovered porphyry Cu deposits in this area makes it attractive for exploration, but the potential for supergene enrichment is low, as volcanic deposition likely terminated supergene processes before significant ore-grade enrichment could occur (Sillitoe and McKee, 1996; Sillitoe, 2005).

This paper presents a way of tracking exhumation by dating and determining the emplacement depth of outcropping granitoid plutons: the average exhumation rate can simply be calculated as the emplacement depth divided by the time interval between emplacement and arrival at the surface (or near-surface). The latter can be constrained by supracrustal cover rocks in depositional contact with the pluton or by dated supergene minerals that constrain the time at which a pluton reached the subsurface water table. Unlike thermochronology-based exhumation studies conducted in the region (Maksaev and Zentilli, 1999; McInnes et al., 1999; Barnes and Ehlers, 2009; Juez-Larré et al., 2010; Reiners et al., 2015; Avdievitch et al., 2018; Sanchez et al., 2018; Stalder et al., 2020), this approach does not require knowledge of the geothermal gradient and its fluctuations through time, which can be difficult to accurately model, particularly in terranes experiencing simultaneous exhumation and magmatism (Murray et al., 2018).

New U-Pb zircon laser ablation-inductively coupled plasma-mass spectrometry (LA-ICP-MS) ages of 49 intrusive rocks (43 plutons and six porphyries) from the middle Eocene-early Oligocene metallogenic belt in the Precordillera of northern Chile between 17.8° and 24.2°S (Fig. 1B) were obtained. The intrusions represent four different age groups: Carboniferous-Permian, Triassic, Late Cretaceous-Paleocene, and Eocene. Detailed petrography and whole-rock geochemistry identified a subset of 20 pluton samples suitable for Al-in-hornblende geobarometry, and emplacement depths were determined using the calibration of Mutch et al. (2016). When combined with minimum exposure ages from supracrustal cover rocks or nearby supergene mineralization, an average exhumation rate was determined for each pluton. In this way we were able to deduce a 300-m.y. history of exhumation and burial along this segment of the Precordillera and constrain average exhumation rates during periods of hypogene and supergene mineralization.

Geologic Background

Tectonomagmatic evolution of northern Chile

Northern Chile, situated on the western margin of the Central Andes, comprises six morphotectonic units: Coastal Cordillera, Central depression, Precordillera, Western Cordillera, and the Altiplano and Puna plateaus (Fig. 1A). The region has experienced active subduction since at least the Ordovician, which has given rise to several magmatic arcs (Charrier et al., 2007; Niemeyer et al., 2018). Ordovician rocks are sparse, but the Carboniferous to Triassic arcs are well represented in the Precordillera by large intrusions (Fig. 1B) and their volcanic counterparts (Maksaev et al., 2014, and references therein). Slab rollback and possible steepening of the subduction angle in the Triassic caused extension in the overriding plate and eventually a westward shift in arc magmatism, commencing in the Coastal Cordillera in the Jurassic (del Rey et al., 2016; Oliveros et al., 2020). A marine back-arc basin developed in the present-day Central depression and Precordillera at this time (Vicente, 2006). The magmatic arc migrated progressively eastward from the Coastal Cordillera due to subduction erosion at the continental margin and progressive shallowing of the subduction angle (Kukowski and Oncken, 2006), generating volcanic and plutonic rocks with an eastward-younging trend (Coira et al., 1982). By the Eocene, the arc had reached the Precordillera, and intrusive rocks were emplaced into dominantly Jurassic-Cretaceous and Carboniferous-Triassic stratigraphic units (e.g., Tomlinson et al., 2001). Since the late Oligocene, the main axis of the magmatic arc has lain in the Western Cordillera, but in many locations volcanic deposits from this arc unconformably overlie the Eocene-Oligocene arc in the Precordillera, particularly north of ~19.5° S (García et al., 2004, 2017; van Zalinge et al., 2016; Platzman et al., 2020).

Several orogenic events have affected northern Chile since the Carboniferous. The middle Permian San Rafael orogenic event (Rapalini, 1989; Llambías and Sato, 1990) caused major reorganization of fault-bounded crustal blocks in the Precordillera (Tomlinson et al., 2001, 2012; Tomlinson and Blanco, 2008), before a long, dominantly extensional period from the Triassic to the middle Eocene. During this period, abundant supracrustal units were deposited in the Central depression and Precordillera, first in the Jurassic-Early Cretaceous marine back-arc basin and later in continental basins (Tomlinson et al., 2001; Cornejo et al., 2003; Charrier et al., 2007). The extensional regime was interrupted by the Late Cretaceous Peruvian (Mégard, 1987; Scheuber et al., 1994) and K-T (Cornejo et al., 2003) orogenic events, which produced

Fig. 1. A. Digital elevation model of northern Chile showing the six morphotectonic units, major sedimentary basins, the Domeyko fault system, the Antofagasta-Calama lineament, and Precordilleran structural domains referred to in the text. Structural features are compiled from Tomlinson et al. (2001), Bouzari and Clark (2002), SERNAGEOMIN (2003), Charrier et al. (2007), and Mpodozis and Cornejo (2012). Morphotectonic units and major sedimentary basins are modified from Charrier et al. (2007), Barnes and Ehlers (2009), and Evenstar et al. (2017). Locations of intrusive rocks sampled in this study are shown, with sample numbers given in B. The dashed box shows the extent of the maps in Figures 1B, 10, and 12. B. Outcropping intrusive rocks and locations of samples draped over a shaded relief map. A selection of Permian-Triassic and middle Eocene-early Oligocene porphyry Cu deposits is shown, defining the trajectories of the overlapping Permian-Triassic and middle Eocene-early Oligocene metallogenic belts. Intrusion outcrops are modified after SERNAGEOMIN (2003) and locations of porphyry Cu deposits after Marquardt et al. (1997), Tomlinson et al. (2001), Munizaga et al. (2008), Singer et al. (2008), and Mpodozis and Cornejo (2012).

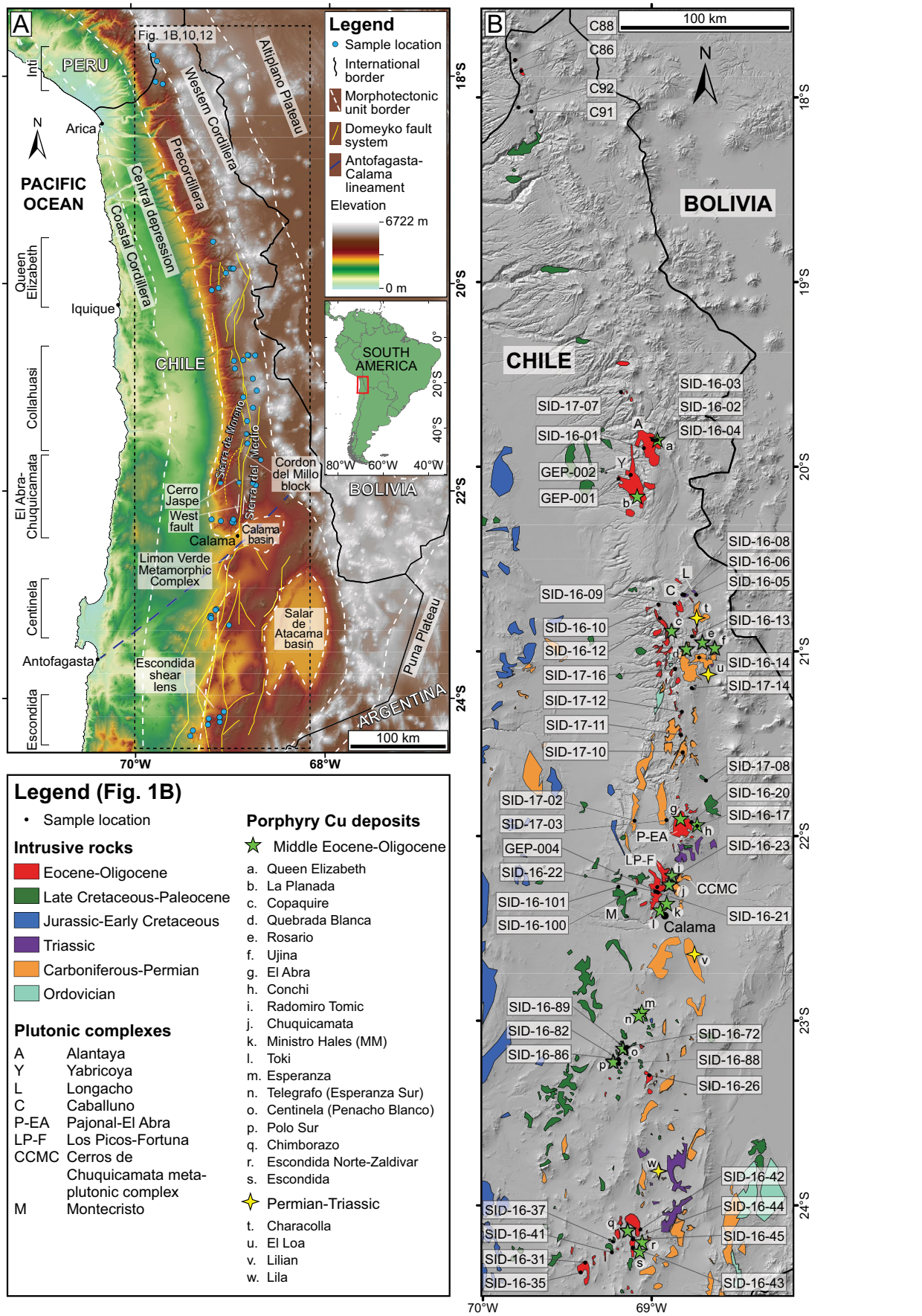

regional unconformities. The Andean orogeny (Eocene to Present), which is dominated by tectonic shortening, crustal thickening, mountain building, and exhumation (Maksaev and Zentilli, 1999; Haschke et al., 2002; Armijo et al., 2015), commenced with the Incaic orogenic event between ~45 and ~33 Ma (Tomlinson et al., 2001; Mpodozis and Cornejo, 2012). The Precordillera at this time was bounded to the east and west by two arc-parallel thrust fault systems with opposite vergence, causing pop-up-style uplift and significant erosion of the range (Maksaev and Zentilli, 1999; Mpodozis et al., 2005; Amilibia et al., 2008; Charrier et al., 2013; Armijo et al., 2015; Reiners et al., 2015). Around 2–3 km of surface uplift of the Western Cordillera and Precordillera relative to the Central depression has taken place since the Incaic orogenic event (Armijo et al., 2015) in a tectonic regime that has remained largely compressional with several deformational peaks (Kay et al., 1999).

Patterns of exhumation

In the area around Chuquicamata (Fig. 1B), rock units representing contrasting Carboniferous-Permian paleodepths occur in different fault-bounded structural domains (Tomlinson et al., 2001, 2012; Tomlinson and Blanco, 2008). Erosional contacts with Triassic supracrustal rocks indicate juxtaposition and exposure of these different paleodepths by this time. This suggests that a period of exhumation occurred between the Permian and Triassic, possibly correlated with the San Rafael orogenic event, during which spatially variable exhumation rates prevailed (Tomlinson et al., 2012). In Sierra del Medio and at Cerro Jaspe (Fig. 1A), Carboniferous-Permian rocks are dominantly supracrustal units intruded by epizonal granitoids. The Cerros de Chuquicamata metaplutonic complex (Fig. 1B) represents a deeper crustal level with schistose and gneissic Carboniferous-Permian granitoids. Close to Chuquicamata, high-pressure metamorphism of the Limón Verde metamorphic complex (Fig. 1A) reached 13 ± 1 kbar at 270 ± 12 Ma (Lucassen et al., 1999), providing clear evidence for deep Permian burial in this location. It has also been suggested that Sierra de Moreno represents a deeper crustal level than Sierra del Medio, based on exposed basement consisting of Precambrian protoliths metamorphosed to amphibolite (and locally granulite) facies in the Cambrian-Ordovician (Damm et al., 1990; Tomlinson et al., 2001; Loewy et al., 2004).

Regional low-temperature thermochronology studies of Cenozoic exhumation in the Central Andes using zircon and apatite fission track (ZFT and AFT) and zircon and apatite (U-Th)/He (ZHe and AHe) analyses have consistently identified an eastward-younging trend in cooling ages (Barnes and Ehlers, 2009; Reiners et al., 2015; Stalder et al., 2020). This has been interpreted as reflecting an eastward progression of exhumation, starting in the Precordillera and Western Cordillera between ~60 and 40 Ma and propagating to the eastern side of the Altiplano and Puna plateaus, where exhumation continues today (Barnes and Ehlers, 2009; Reiners et al., 2015). Based on low-temperature thermochronology and 1-D thermokinematic modeling, two recent studies determined long-term mean exhumation rates in the Precordillera of <0.20 km/m.y. since ~50 Ma (Avdievitch et al., 2018) and 0.25 km/m.y. since ~80 Ma (Stalder et al., 2020). Neither study can, however, rule out a pulsed exhumation history with periods of higher rates. Maksaev and Zentilli (1999) used AFT analysis to determine rates of 0.10–0.20 km/m.y. from 50 to 30 Ma associated with the Incaic orogenic event, and ~0.05 km/m.y. from 30 Ma to present. Sanchez et al. (2018) estimated <2.5 km of exhumation in the Centinela district since the early Oligocene, based on AHe ages, yielding an exhumation rate of <~0.09 km/m.y. since then. They also infer that rates were higher than this during the Incaic orogenic event. Lower exhumation rates from at least the early Miocene onward are supported by widespread exposed Eocene plutons (e.g., Tomlinson et al., 2001) alongside late Oligocene-early Miocene supracrustal units, such as exceptionally well preserved ignimbrites (van Zalinge et al., 2016). Furthermore, the presence of extensive late Oligocene-Miocene erosion surfaces (pediplains) across northern Chile (Galli-Olivier, 1967; Mortimer, 1973; Dunai et al., 2005; Kober et al., 2007; Bissig and Riquelme, 2009; Evenstar et al., 2017) suggest decreased exhumation rates from this time onward (Riquelme et al., 2017; Carretier et al., 2018; Sanchez et al., 2018). This is consistent with a compilation by Carretier et al. (2018) of erosion rates across Chile north of 27°S, over shorter time spans of <100 years (from suspended sediments or short-lived isotopes), 100–100,000 years (cosmogenic nuclides, lacustrine sediment budgets), and <~20 m.y. (cosmogenic nuclides), which are predominantly less than 0.01 km/m.y. These determinations are generally taken from gently sloping surfaces; erosion rates an order of magnitude higher occur locally where slopes are steeper, such as in rivers with steep knickzones or on volcanic edifices (Carretier et al., 2018, and references therein).

The long-term exhumation rates determined for northern Chile are relatively low for an orogenic belt—at least 10 times lower than the highest rates observed in the Himalayas (e.g., Thiede and Ehlers, 2013; Adams et al., 2015). This difference has been attributed to the arid climate that has prevailed in the region since the Triassic or Jurassic (Hartley et al., 2005; Clarke, 2006). The present hyperarid climate is thought to have persisted since at least the middle-late Miocene (Mortimer, 1973; Alpers and Brimhall, 1988; Sillitoe and McKee, 1996; Jordan et al., 2014; Cooper et al., 2016; Rech et al., 2019) and possibly since the late Oligocene (Dunai et al., 2005; Evenstar et al., 2009, 2017). Rates of weathering and erosion in modern hyperarid climates are orders of magnitude lower than in more humid regions (Jordan et al., 2014, and references therein), which could explain the extremely low Miocene-Recent erosion rates.

Hypogene ore formation in the Precordillera

Northern Chile hosts two major porphyry Cu belts: the Paleocene-early Eocene belt, which mainly occupies the eastern part of the Central depression, and the middle Eocene-early Oligocene belt in the Precordillera. Additional porphyry Cu deposits associated with Permian-Triassic and Middle Jurassic-Cretaceous magmatism are of minor economic importance (Sillitoe and Perelló, 2005; Maksaev et al., 2007; Zentilli et al., 2018, and references therein). The Permian-Triassic and middle Eocene-early Oligocene belts are superimposed, and both occur within the study area (Fig. 1B). The middle Eocene-early Oligocene belt hosts some of the largest porphyry Cu deposits in the world, including Chuquicamata, Escondida,

and Rosario (e.g., Sillitoe and Perelló, 2005). The Permian-Triassic porphyry Cu deposits have characteristics resembling their younger counterparts and do not seem to differ in terms of level of exposure but lack sufficient metal endowment to be economically viable (Cornejo et al., 2019). Hypogene mineralization in the younger belt took place between ~45 and ~31 Ma, and many deposits formed along strike-slip faults of the Domeyko fault system (Fig. 1A; Reutter et al., 1991, 1996; Lindsay et al., 1995; Cornejo et al., 1997; Sillitoe and Perelló, 2005, and references therein; Mpodozis and Cornejo, 2012). Several of the deposits have ore reserves exceeding 1 Gt and high hypogene Cu grades (Sillitoe and Perelló, 2005). The bulk of the ore is typically hosted within the early formed sulfide assemblage of chalcopyrite, pyrite, bornite, and molybdenite, associated with potassic alteration in the cores of the systems, but the highest Cu grades commonly occur where a late-stage high-sulfidation assemblage associated with phyllic and/or advanced argillic alteration is telescoped onto the potassic assemblage during rapid exhumation (Sillitoe, 1994, 1999; Masterman et al., 2005; Hervé et al., 2012; Maydagán et al., 2015; Sillitoe et al., 2019). Prime examples include Chuquicamata (Ossandón et al., 2001), Rosario (Masterman et al., 2005), Escondida (Padilla Garza et al., 2001; Hervé et al., 2012), Ministro Hales (Sillitoe et al., 1998; Boric et al., 2009), and Escondida Norte-Zaldivar (Hervé et al., 2012; Fig. 1B).

Supergene enrichment in the Precordillera

The middle Eocene-early Oligocene metallogenic belt hosts several world-class supergene enrichment zones (Sillitoe, 2005). Favorable conditions for enrichment require a balance between exhumation and relative water table descent, allowing enough time for Cu to be leached and transported down to the water table before it is lost at the surface (Emmons, 1917; Brimhall et al., 1985; Hartley and Rice, 2005; Sillitoe, 2005; Riquelme et al., 2017). Most major mature enrichment zones developed over 3–9 m.y. of supergene activity (Sillitoe, 2005) and are thought to require relatively stable landscapes and low exhumation rates, like those that prevail in semiarid to arid regions during pediplain formation (Bouzari and Clark, 2002; Riquelme et al., 2017; Sanchez et al., 2018).

However, exhumation rate is not the only factor affecting supergene enrichment. The presence of pyrite is essential, since the sulfuric acid generated by pyrite oxidation drives further leaching and Cu transport. Host rocks with low acid-buffering capacity help keep Cu in solution and prevent precipitation of Cu oxide minerals above the water table (Emmons, 1917; Chávez, 2000; Sillitoe, 2005; Reich and Vasconcelos, 2015). Rock permeability, which enables efficient descent of solutions, and the presence of bacteria that facilitate sulfide oxidation, sulfate reduction, and metal adsorption are also crucial (Sillitoe, 2005, and references therein; Enders et al., 2006).

The timing of supergene enrichment in northern Chile has generally been constrained via K-Ar and $^{40}Ar/^{39}Ar$ dating of the K-bearing sulfate mineral alunite ($KAl_3(SO_4)_2(OH)_6$), which forms in the acidic conditions resulting from pyrite oxidation (Vasconcelos, 1999). Early studies in northern Chile found alunite ages ranging from ~34 to ~14 Ma and linked the cessation of alunite formation to the onset of hyperaridity, which reduced available meteoric water to drive enrichment (Alpers and Brimhall, 1988; Sillitoe and McKee, 1996). Subsequent studies have broadened this age range to ~44–~5 Ma (Marsh et al., 1997; Mote et al., 2001; Rowland and Clark, 2001; Bouzari and Clark, 2002; Perelló, 2003; Quang et al., 2003, 2005; Arancibia et al., 2006; Bissig and Riquelme, 2010; Riquelme et al., 2017). The oldest ages (>~25 Ma) derive from the Paleocene-early Eocene metallogenic belt, where deposits were unroofed earlier than in the middle Eocene-early Oligocene belt (Sillitoe and McKee, 1996), and experienced favorable conditions for supergene enrichment during the Incaic orogenic event, which mainly affected the Precordillera (Bouzari and Clark, 2002; Maksaev and Zentilli, 1999). The youngest supergene ages are found in southern Peru and to the south of our study area (~26°S), which were likely the last areas affected by desiccation (Arancibia et al., 2006). Supergene ages within our study area define a supergene window between ~25 and ~12 Ma, during which conditions were favorable for supergene enrichment.

Sample Set

Forty-nine samples from intrusive rocks (43 from plutons and 6 from porphyries) were collected over an ~730-km-long segment (17.8°–24.2°S) of the middle Eocene-early Oligocene metallogenic belt (Fig. 1). The study area is split into six sections, each named after a major porphyry Cu deposit or district within it, apart from Inti, a name given by BHP to the area close to the border with Peru (Fig. 1A), which contains only minor, subeconomic Eocene mineralization (Ataspaca stockwork and skarn on the Peruvian side of the border; Clark et al., 1990).

Sampling focused on outcropping unaltered felsic granitoid rocks, which were the most abundant intrusive rock type in most parts of the study area. Samples were mainly collected from Eocene plutons, but Carboniferous-Permian, Triassic, and Late Cretaceous-Paleocene plutons were also sampled. Eocene mineralized porphyries were sampled at the Queen Elizabeth, Conchi, and Centinela deposits as well as from the San Lorenzo porphyries within the Los Picos-Fortuna pluton. A Triassic mineralized porphyry dike was sampled within the Caballuno pluton north of the Collahuasi district (Fig. 1B). Samples C91 and C92 were collected from exploration holes in the Inti region at depths of 1,272 and 947 m, respectively, immediately beneath the thick Oxaya Formation ignimbrites.

Petrography

Detailed thin section examination of each sample combined with point counting analysis (1,000 points per thin section) established that the plutons range in composition from quartz gabbro to monzogranite (Fig. 2). Representative images of the different age groups and areas are shown in Figure 3A-J. Mineralized porphyries are heavily altered, with an aphanitic matrix. Therefore, apart from the relatively coarse grained sample SID-16-23 from the San Lorenzo porphyries, they were not point counted, and classification is based on estimated primary phenocryst proportions and grain size. Complete petrographic descriptions can be found in Appendix 1; general features are summarized below.

All samples contain the major primary mineral phases plagioclase, quartz, and K-feldspar in variable proportions, with minor and accessory zircon, apatite, and Fe-Ti oxides

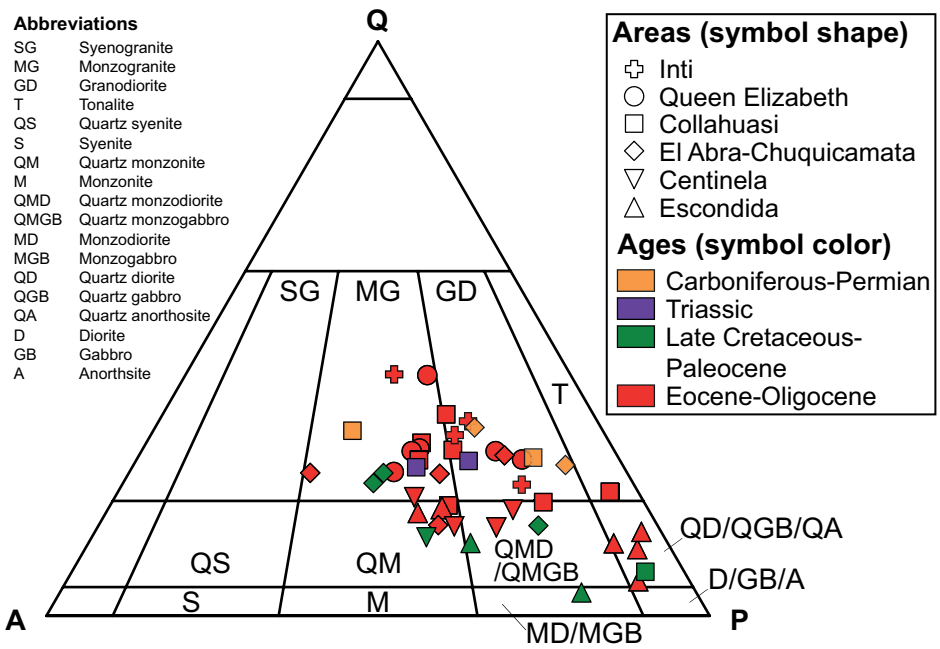

Fig. 2. Quartz-alkali feldspar-plagioclase (QAP) classification of the 43 studied pluton samples based on point counting.

(Table 1). Most samples contain biotite and amphibole, but in the Centinela and Escondida areas, clinopyroxene tends to be the dominant mafic mineral. Titanite occurs as a minor phase in some samples. In all but one sample, K-feldspar is orthoclase with or without thin, poorly developed, perthite exsolution lamellae. Carboniferous-Permian granodiorite sample SID-17-02 from Sierra de Moreno contains microcline K-feldspar (Fig. 3F), which may reflect slow cooling. Granophyric intergrowths between K-feldspar and quartz occur occasionally (Fig. 3H). The order of crystallization of the major phases is generally as follows: plagioclase (± clinopyroxene where present) > amphibole, biotite > interstitial quartz and K-feldspar. K-feldspar is typically the last phase to crystallize and, in clinopyroxene-rich rocks of the Escondida area, commonly occurs as poikilocrysts enclosing mafic minerals and plagioclase (Fig. 3J).

Of the pre-Eocene plutons, the Carboniferous-Permian age group was sampled in four locations within the Collahuasi and El Abra-Chuquicamata areas. Samples comprise relatively coarse grained (0.5–4 mm), hypidiomorphic hornblende-biotite granodiorites and granites, typically coarser than samples from the other age groups. Two Triassic samples, from the Longacho (SID-16-05) and Caballuno (SID-16-06) plutons (Fig. 1B) in the Collahuasi area, are equigranular, medium-grained (1–3 mm) biotite-hornblende granodiorite and monzogranite, in places containing minor clinopyroxene, commonly rimmed by hornblende. Petrographically, these plutons strongly resemble neighboring intrusions of Eocene age. Late Cretaceous-Paleocene plutons sampled from seven locations in the Collahuasi, El Abra-Chuquicamata, Centinela, and Escondida areas vary between quartz gabbro and monzogranite. Hornblende and biotite are the dominant mafic minerals in the medium- to coarse-grained plutons of Collahuasi and El Abra-Chuquicamata, whereas clinopyroxene is more common in the finer-grained, sometimes porphyritic, plutons of Centinela and Escondida.

Thirty Eocene pluton samples were collected across all six areas and range in composition from quartz diorite to monzogranite. In general, they are coarser grained and more felsic in the northern areas of Inti to El Abra-Chuquicamata than in

Fig. 3. Representative hand sample and thin section images of plutonic rocks used in this study. A. Carboniferous granodiorite SID-17-03 from Cerro Jaspe (El Abra-Chuquicamata area). B. Triassic granodiorite SID-16-05 (Collahuasi area). C. Paleocene quartz monzonite SID-16-72 (Centinela area). Primary clinopyroxene is completely replaced by secondary actinolite. Primary amphibole shows breakdown rims. D. Eocene granodiorite SID-16-01 from the Alantaya pluton (Queen Elizabeth area). E. Eocene quartz diorite SID-16-45 (Escondida area). F. Carboniferous granodiorite SID-17-02 from Sierra de Moreno (El Abra-Chuquicamata area). Photomicrograph under cross-polarized light (XPL) shows a microcline K-feldspar grain with typical crosshatch twinning. G. Eocene granodiorite SID-16-02 from the Alantaya pluton (Queen Elizabeth area). Photomicrograph (XPL) shows hypidiomorphic granular texture. H. Eocene quartz monzonite SID-16-13 (Collahuasi area). Photomicrograph (XPL) of granophyric texture. I. Eocene monzogranite SID-16-26 (Centinela area). Photomicrograph in plane-polarized light (PPL) of miarolitic cavity with euhedral quartz crystals growing from its walls and a late epidote infill. J. Late Cretaceous monzodiorite SID-16-37 (Escondida area). Photomicrograph (XPL) of poikilitic K-feldspar enclosing earlier-crystallized minerals. Mineral abbreviations: Act = actinolite, Bt = biotite, Chl = chlorite, Cpx = clinopyroxene, Ep = epidote, Hbl = hornblende, Kfs = alkali feldspar, Mag = magnetite, Opx = orthopyroxene, Pl = plagioclase, Qz = quartz.

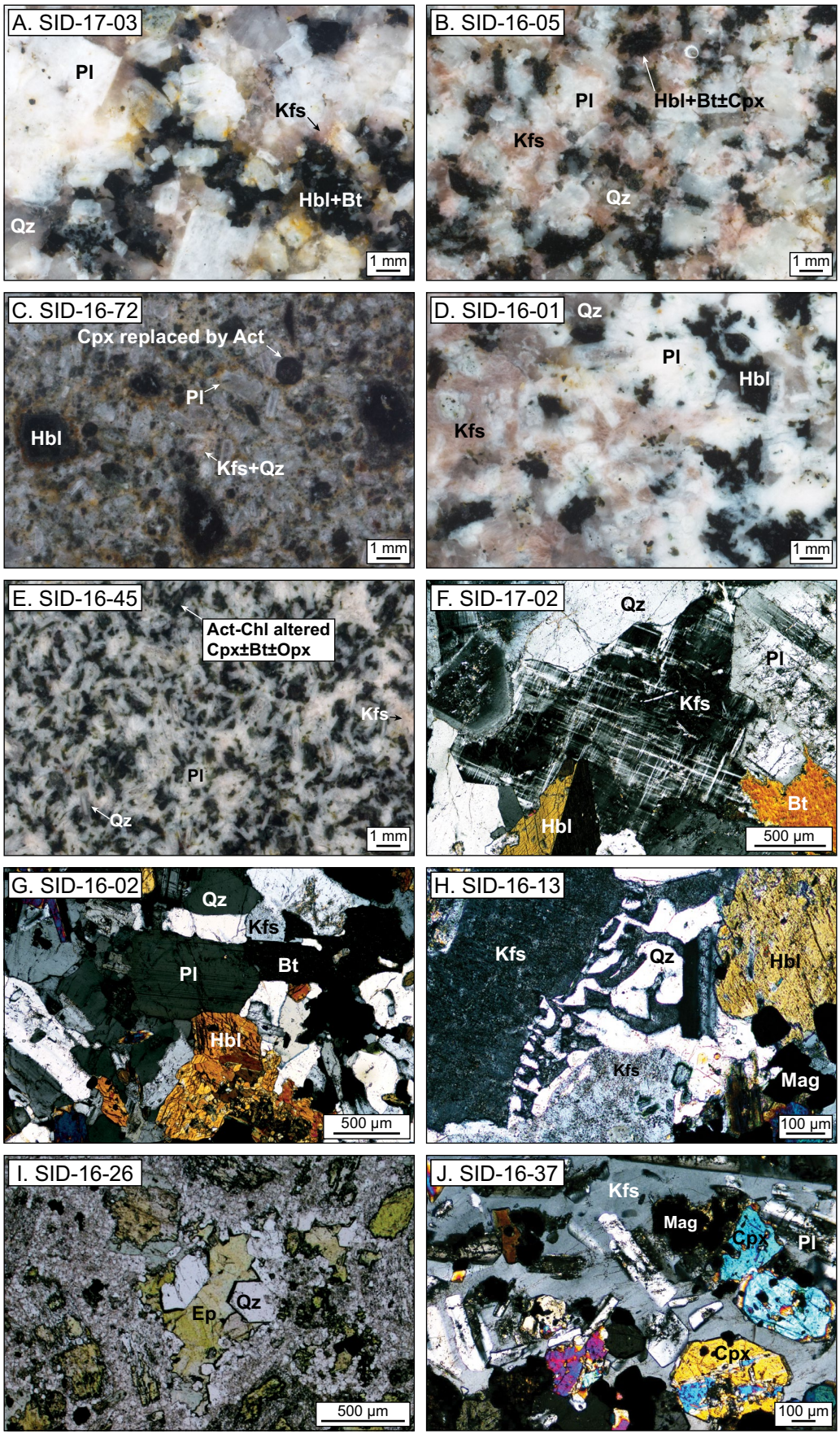

Table 1. Sample Locations, Rock Types, and Modal Mineralogies Determined by Point Counting

Sample	Area	Latitude (decimal degrees)	Longitude (decimal degrees)	Rock type	Modal mineralogy (vol %) Primary minerals Pl	Qz	Kfs	Bt	Hbl	Cpx	Ox	Ap	Ttn	Zrn	Alteration minerals[1] Act	Chl	Ep	Cal	Hole/ unknown
C88	Inti	–17.80228	–69.77401	Monzogranite	30.2	39.8	25.2	3.5			0.2	1.1							
C86	Inti	–17.86093	–69.73832	Granodiorite	42.8	29.0	21.0	6.5			0.7								
C92	Inti	–18.05827	–69.75440	Granodiorite	38.4	27.5	15.9	9.7	4.1		0.8	1.4	0.9			1.3			
C91	Inti	–18.08077	–69.68177	Granodiorite	50.4	18.8	14.0	9.8	4.4	1.2	1.4								
SID-17-07	Queen Elizabeth	–19.60263	–69.17526	Monzogranite	35.4	24.3	24.5	0.4	0.3	0.2	2.8		0.2		5.7	6.2			
SID-16-02	Queen Elizabeth	–19.86910	–68.99434	Granodiorite	48.8	22.5	12.2	5.9	9.2		1.4								
SID-16-04	Queen Elizabeth	–19.86970	–68.96774	Quartz-feldspar porphyry	N/A	N/A	N/A	N/A	N/A	N/A	N/A	N/A	N/A	N/A	N/A	N/A	N/A	N/A	N/A
SID-16-03	Queen Elizabeth	–19.87319	–68.97989	Granodiorite	46.4	24.6	15.4	6.8	5.4		1.3		0.1						
SID-16-01	Queen Elizabeth	–19.91406	–69.04462	Monzogranite	35.7	22.0	31.1		9.6		1.4			0.2					
GEP-002	Queen Elizabeth	–20.05135	–69.11980	Monzogranite	33.8	38.2	19.8	4.6	1.8		1.0	0.4	0.2	0.2					
GEP-001	Queen Elizabeth	–20.07255	–69.19003	Monzogranite	35.0	24.2	26.0	1.6	3.8	3.6	3.8						1.7	0.3	
SID-16-08	Collahuasi	–20.70641	–68.82264	Feldspar porphyry	N/A	N/A	N/A	N/A	N/A	N/A	N/A	N/A	N/A	N/A	N/A	N/A	N/A	N/A	N/A
SID-16-05	Collahuasi	–20.70848	–68.74363	Granodiorite	43.8	23.4	20.0	4.0	6.2	1.0	1.4							0.2	
SID-16-06	Collahuasi	–20.70879	–68.81128	Monzogranite	35.8	21.6	26.2	4.9	6.3	0.6	2.1	1.0	0.8						0.7
SID-16-09	Collahuasi	–20.75652	–68.86755	Granodiorite	37.4	30.2	19.2	5.0	6.8		0.9	0.3	0.2						
SID-16-10	Collahuasi	–20.76095	–68.96118	Tonalite	55.2	15.8	3.1	2.7	0.2	0.7	3.6				5.4	11.6	0.7	1.0	
SID-16-12	Collahuasi	–20.83632	–68.95201	Monzogranite	35.8	25.5	24.2	1.0	8.1	1.0	2.2	0.4	0.8						1.0
SID-16-13	Collahuasi	–20.93429	–68.76729	Quartz monzonite	37.7	13.9	21.8	6.6	11.1		3.3	1.2	1.3						3.1
SID-16-14	Collahuasi	–21.04880	–68.72541	Granodiorite	52.0	24.0	11.2	6.9	4.4		1.2								0.3
SID-17-16	Collahuasi	–21.10428	–68.86424	Granodiorite	37.4	22.6	19.1	9.8	9.3	0.1	1.5		0.2						
SID-17-14	Collahuasi	–21.20594	–68.76450	Quartz gabbro	47.5	3.8	3.4	1.8	38.2	1.4	2.8	0.2	0.2				0.3	0.4	
SID-17-12	Collahuasi	–21.33480	–68.82481	Quartz monzodiorite	53.6	16.0	12.4	6.8	8.8		2.0	0.2					0.2		
SID-17-11	Collahuasi	–21.45819	–68.83142	Monzogranite	38.4	24.0	27.0	4.8	2.2	1.6	2.0								
SID-17-10	Collahuasi	–21.55131	–68.82207	Monzogranite	28.0	30.0	35.2	2.6	2.8	0.1	1.3								
SID-17-08	El Abra-Chuqui.	–21.70661	–68.68488	Quartz monzodiorite	51.6	11.6	14.2	4.8	14.1		1.8	0.4	0.2	0.2			1.0	0.1	
SID-17-03	El Abra-Chuqui.	–21.92116	–68.91385	Granodiorite	41.6	28.3	16.5	7.2	5.1		0.7		0.4				0.2		
SID-17-02	El Abra-Chuqui.	–21.92523	–69.09896	Granodiorite	53.4	21.5	7.1	11.0	6.0		0.8			0.2					
SID-16-20	El Abra-Chuqui.	–21.94034	–68.76780	Granodiorite	50.5	25.2	15.4	1.9	4.6		2.2		0.2						
SID-16-17	El Abra-Chuqui.	–21.96175	–68.73559	Quartz-feldspar porphyry	N/A	N/A	N/A	N/A	N/A	N/A	N/A	N/A	N/A	N/A	N/A	N/A	N/A	N/A	N/A
SID-16-101	El Abra-Chuqui.	–22.29112	–69.19343	Monzogranite	33.2	20.7	31.8	3.8	9.1		1.2	0.2							
SID-16-23	El Abra-Chuqui.	–22.29269	–68.96686	Monzogranite porphyry	40.8	21.1	24.4	8.0	4.9		0.6						0.2		
SID-16-100	El Abra-Chuqui.	–22.30720	–69.09734	Monzogranite	32.0	18.8	33.2	5.6	7.8		2.4	0.2							
SID-16-22	El Abra-Chuqui.	–22.31666	–68.97967	Quartz monzonite	42.2	12.7	27.0	2.4	13.4	0.4	1.7	0.2							
GEP-004	El Abra-Chuqui.	–22.31855	–68.97034	Granodiorite porphyry	N/A	N/A	N/A	N/A	N/A	N/A	N/A	N/A	N/A	N/A	N/A	N/A	N/A	N/A	N/A
SID-16-21	El Abra-Chuqui.	–22.32276	–68.96210	Monzogranite	23.2	20.6	40.0	6.0	7.5		1.4	1.1	0.2						
SID-16-72	Centinela	–23.15713	–69.14464	Quartz monzonite	39.1	10.0	27.9		3.0	7.1	3.8				3.6	5.5			
SID-16-89	Centinela	–23.16612	–69.15368	Quartz-feldspar porphyry	N/A	N/A	N/A	N/A	N/A	N/A	N/A	N/A	N/A	N/A	N/A	N/A	N/A	N/A	N/A
SID-16-82	Centinela	–23.22098	–69.20368	Quartz monzodiorite	48.6	12.2	19.6	0.8		3.8	3.6				3.5	5.8	2.1		
SID-16-86	Centinela	–23.22203	–69.20318	Quartz monzonite	46.2	13.1	26.2	4.8		1.4	2.9				3.6	1.4	0.4		
SID-16-88	Centinela	–23.24578	–69.19980	Quartz monzodiorite	52.5	15.6	17.4	5.1	1.4		2.4				5.6				
SID-16-26	Centinela	–23.31262	–69.01378	Monzogranite	37.0	16.6	27.8	0.8		3.8	1.3				2.2	6.2	4.3		
SID-16-42	Escondida	–24.14710	–69.06620	Quartz diorite	60.1	10.4	2.1	7.0		6.8	2.4	1.2			5.8	3.2		1.0	
SID-16-45	Escondida	–24.20023	–69.11080	Quartz diorite	62.0	4.1	5.5			0.2	3.2				15.2	9.6	0.2		
SID-16-44	Escondida	–24.20086	–69.11102	Quartz diorite	61.2	9.5	6.2			5.8	2.5				3.4	10.8	0.6		
SID-16-37	Escondida	–24.21346	–69.22651	Monzodiorite	54.6	2.3	12.2	2.6		15.2	8.2		0.8		4.1				
SID-16-43	Escondida	–24.24625	–69.10972	Quartz diorite	61.9	8.4	3.7	1.4		6.2	2.4	0.2			5.0	10.6		0.2	
SID-16-41	Escondida	–24.27214	–69.23484	Quartz monzodiorite	50.4	10.3	26.0	3.7		4.2	2.2				2.8			0.4	
SID-16-31	Escondida	–24.32737	–69.39333	Quartz monzonite	43.1	15.6	26.6	3.8	8.7		2.2								
SID-16-35	Escondida	–24.38040	–69.41998	Quartz monzonite	38.2	14.2	28.2			5.8	2.8	0.3			4.0	6.0	0.5		

Samples are listed from north to south; N/A = not applicable

Mineral abbreviations: Act = actinolite, Ap = apatite, Bt = biotite, Cal = calcite, Chl = chlorite, Cpx = clinopyroxene, Ep = epidote, Hbl = hornblende, Kfs = alkali feldspar, Ox = Fe-Ti oxide, Pl = plagioclase, Qz = quartz, Ttn = titanite, Zrn = zircon

[1]Logged only when impossible to determine precursor primary mineral

the southern areas of Centinela and Escondida. In the Late Cretaceous-Paleocene samples, clinopyroxene is more abundant in plutons of the Centinela and Escondida areas than in those farther north. Clinopyroxene-dominated, more mafic plutons do occur between Inti and Chuquicamata (e.g., SID-16-10, Collahuasi area), but biotite and hornblende are more commonly the dominant mafic minerals. Plutons containing these minerals were sampled preferentially because of their suitability for Al-in-hornblende geobarometry. Eocene plutons tend to be equigranular and hypidiomorphic, but porphyritic textures also occur. Miarolitic cavities containing euhedral quartz crystals growing from the walls and a later infill of epidote ± chlorite occur in the Centinela (sample SID-16-26; Fig. 3I) and Queen Elizabeth (sample GEP-001, Yabricoya pluton) areas. Miarolitic cavities likely indicate shallow epizonal emplacement depths (Candela, 1997), but there is no definitive pressure limit for their formation.

Most plutons have experienced secondary alteration, but its intensity varies greatly between samples. The style of alteration is generally propylitic, represented by sericite-altered feldspar, chlorite-altered biotite, and hornblende and pyroxene replaced by actinolite ± chlorite. Epidote-altered mafic minerals and calcite occur locally. Clinopyroxene-bearing samples tend to be the most intensely altered, particularly Eocene samples from the Escondida area, where the mafic minerals have been completely replaced by actinolite and chlorite. In Centinela sample SID-16-88, some hornblendes have been partly replaced by biotite instead of actinolite ± chlorite, indicative of higher-temperature potassic, rather than propylitic, alteration. Also, in some porphyry samples relict hornblende has been completely replaced by shreddy biotite (samples SID-16-08, SID-16-23, and GEP-004). In some mineralized porphyries, phyllic (quartz-sericite-pyrite) alteration locally overprinted earlier potassic-altered zones (e.g., Conchi sample SID-16-17).

Geochemistry

Powders of <25-μm grain size were prepared for each sample at the University of Bristol by milling a portion of ~2 kg of crushed material in a Si_3N_4 ball mill. For major and minor element oxide determinations, rock powders were mixed with a flux in known proportions, then melted in Pt crucibles, poured into a Pt casting dish, and quenched into fusion beads for analysis by X-ray fluorescence using a Panalytical Axios Advanced spectrometer at the University of Leicester. A fraction of each powder was also heated in a 950°C furnace for 1–1.5 h to determine loss on ignition. However, analysis of sulfide-bearing, mineralized porphyry samples may damage the Pt equipment used to prepare the fusion beads. Therefore, the only analyzed porphyry sample is the weakly mineralized SID-16-23 from the San Lorenzo porphyry in the Los Picos-Fortuna pluton, where the Cu-bearing minerals occur in oxidized form (mainly chrysocholla). Accuracy (±5%) and precision (<2% 2SD) were determined by analyzing reference materials. Analytical results are presented in Appendix 2.

The sampled plutons range between ~50 and ~75 wt % SiO_2 (normalized to 100% anhydrous) and geochemically resemble intrusive rocks elsewhere in this part of the Precordillera (Fig. 4). In Harker diagrams, the plutons mostly plot within the fields delineated by volcanic rocks erupted in the Andean arc between 17° and 25°S (data from http://georoc.mpch-mainz.gwdg.de/georoc/), showing that the plutons likely represent liquid compositions rather than cumulates. K_2O behaves as an incompatible element in the suite, showing a general increase with increasing SiO_2, in agreement with the observation that K-feldspar in most samples is the last phase to crystallize. Samples from the Late Cretaceous-Paleocene group commonly exhibit higher K_2O contents than the general trend—a signature previously attributed to derivation from mafic magmas generated in an extensional setting by low degrees of partial melting of the mantle wedge inboard of the Late Cretaceous-Paleocene arc (Richards et al., 2001; Haschke et al., 2002; Ireland, 2010). The most SiO_2-rich published data from (or near to) mineralized porphyries also tend to plot at higher K_2O than the trend defined by the volcanic rocks, likely due to potassic alteration. Al_2O_3, FeO^T, TiO_2, and P_2O_5 decrease with increasing SiO_2 and therefore behave as compatible elements. The lack of a fractionation peak for P_2O_5 indicates that apatite was saturated throughout crystallization. This, together with overall lower P_2O_5 concentrations, suggests relatively cool magmas compared to the volcanic rocks, since apatite solubility decreases with decreasing temperature (Chappell et al., 2004).

Zircon U-Pb Geochronology

Methodology

Zircons were separated from the 49 samples using conventional heavy mineral separation techniques. Around 100–150 zircons were picked randomly from each sample to reflect the true distribution of grain sizes and morphologies. Grains were mounted in epoxy resin, polished, and imaged at the University of Bristol using a Centaur cathodoluminescence (CL) detector on a Hitachi S-3500N scanning electron microscope to investigate the internal morphology of the crystals, with particular focus on different growth zones.

Zircons were analyzed by LA-ICP-MS U-Pb geochronology at the Geochronology and Tracers Facility, British Geological Survey, Keyworth, using a Nu Instruments, Nu Plasma HR, multicollector-inductively coupled plasma-mass spectrometer (MC-ICP-MS). Laser sampling was performed with a New Wave Research 193ss laser ablation system. Zircon reference material 91500 was used as primary reference material and analyzed at regular intervals during each session. Two other zircon reference materials (GJ1 and either Plesovice or Mud Tank) were also analyzed during each session as secondary and tertiary validation materials.

Grains were randomly selected for analysis, but continuous growth zones on grain rims were targeted in order to sample the youngest domains of the crystal and, hence, the best approximation of the emplacement age. Around 20–30 zircon grains were analyzed per sample.

Data were processed using the Iolite software package (Paton et al., 2011), and weighted mean interpretations were calculated using $^{206}Pb/^{238}U$ isotope ratios rather than dates (Horstwood et al., 2016), after rejecting all data points with >5% discordance between the $^{206}Pb/^{238}U$ and $^{207}Pb/^{235}U$ systems and the inbuilt rejection criteria for $^{206}Pb/^{238}U$ weighted mean dates in Isoplot 4.15 (Ludwig, 2012). Components relating to the systematic uncertainty of the method were

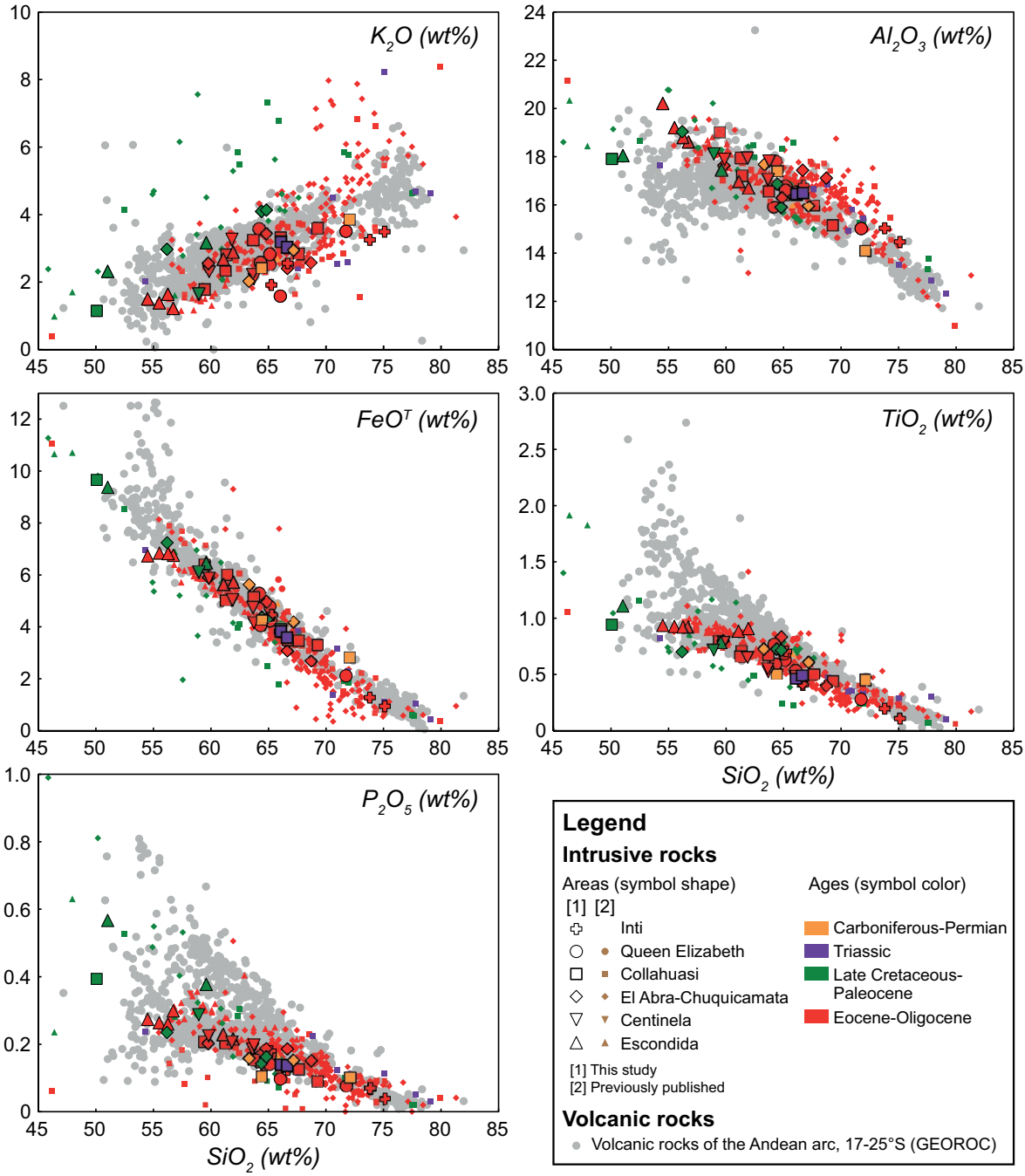

Fig. 4. Harker plots comparing whole-rock data from this study with published data of intrusive rocks from the same part of the Precordillera, and GEOROC (http://georoc.mpch-mainz.gwdg.de/georoc/) data of volcanic rocks from the Andean arc between 17° and 25°S. All data normalized to 100% on an anhydrous basis. Published data compiled from Rogers and Hawkesworth (1989), Maksaev (1990), Ballard (2001), Richards et al. (2001), Haschke et al. (2002), Masterman (2003), Ireland (2010), Rabbia et al. (2017), and Zentilli et al. (2018).

then added to the analytical uncertainties using an in-house Excel calculation. Finally, the weighted mean isotope ratio interpretations were converted into $^{206}Pb/^{238}U$ ages using the algorithms of Isoplot 4.15 (Ludwig, 2012). Full details of the method are provided in Appendix 3.

Results and U-Pb age interpretations

Age interpretations were derived from weighted mean $^{206}Pb/^{238}U$ dates of the data following the rejection criteria described above. Where the mean squared weighted deviation (MSWD; Wendt and Carl, 1991) of the remaining data points exceeded the statistically acceptable limit for a single population at the 95% confidence level, one or more interpretations that met the acceptable MSWD for the population size were evaluated. Our first weighted mean interpretation includes the youngest data point and the largest data population that

Table 2. Summary of Laser Ablation-Inductively Coupled Plasma-Mass Spectrometry Zircon $^{206}Pb/^{238}U$ Weighted Mean Age Interpretations

		Age interpretations							
Sample	Area	n	WM_1 (Ma)	2σ (Ma)	MSWD	N_1	WM_2 (Ma)	2σ (Ma)	MSWD	N_2
C88	Inti	28	35.26	0.34	1.7	9	36.06	0.47	1.6	6
C86	Inti	29	35.68	0.30	1.6	13	36.24	0.31	1.5	12
C92	Inti	23	50.82	0.32	1.6	17	-	-	-	-
C91	Inti	24	39.86	0.24	1.5	18	-	-	-	-
SID-17-07	Queen Elizabeth	13	46.82	0.75	1.5	9	-	-	-	-
SID-16-02	Queen Elizabeth	21	40.65	0.30	1.7	12	40.98	0.26	1.4	13
SID-16-04	Queen Elizabeth	28	37.95	0.34	1.5	17	38.18	0.33	1.3	16
SID-16-03	Queen Elizabeth	21	40.14	0.19	1.0	17	-	-	-	-
SID-16-01	Queen Elizabeth	20	42.93	0.36	1.6	11	43.14	0.35	1.5	11
GEP-002	Queen Elizabeth	29	41.05	0.30	2.0	7	41.30	0.31	1.8	6
GEP-001	Queen Elizabeth	30	45.17	0.23	0.91	10	-	-	-	-
SID-16-08	Collahuasi	58	236.39	0.86	1.6	19	238.44	0.81	1.5	23
SID-16-05	Collahuasi	25	239.2	1.3	1.3	15	-	-	-	-
SID-16-06	Collahuasi	21	236.0	1.6	1.5	13	-	-	-	-
SID-16-09	Collahuasi	23	45.61	0.31	1.4	13	45.98	0.35	1.7	12
SID-16-10	Collahuasi	21	42.61	0.37	1.2	16	-	-	-	-
SID-16-12	Collahuasi	8	43.94	0.75	1.4	7	-	-	-	-
SID-16-13	Collahuasi	21	45.03	0.33	1.5	14	-	-	-	-
SID-16-14	Collahuasi	21	291.8	1.2	0.98	18	-	-	-	-
SID-17-16	Collahuasi	26	44.49	0.34	1.5	20	44.70	0.31	1.4	21
SID-17-14	Collahuasi	29	69.50	0.66	1.3	21	-	-	-	-
SID-17-12	Collahuasi	33	40.00	0.13	1.5	20	40.17	0.12	1.4	23
SID-17-11	Collahuasi	28	40.99	0.17	1.8	11	41.67	0.18	1.3	8
SID-17-10	Collahuasi	23	303.5	1.8	1.3	22	-	-	-	-
SID-17-08	El Abra-Chuqui.	20	71.38	0.51	1.5	16	-	-	-	-
SID-17-03	El Abra-Chuqui.	30	306.2	1.3	1.1	28	-	-	-	-
SID-17-02	El Abra-Chuqui.	26	314.5	1.7	0.95	25	-	-	-	-
SID-16-20	El Abra-Chuqui.	29	36.80	0.24	1.5	13	37.11	0.26	1.6	12
SID-16-17	El Abra-Chuqui.	30	36.32	0.35	1.7	8	36.47	0.37	1.8	8
SID-16-101	El Abra-Chuqui.	23	66.31	0.42	1.2	20	-	-	-	-
SID-16-23	El Abra-Chuqui.	26	38.33	0.28	1.6	21	38.42	0.27	1.3	18
SID-16-100	El Abra-Chuqui.	28	63.60	0.41	0.49	24	-	-	-	-
SID-16-22	El Abra-Chuqui.	35	42.21	0.12	1.5	26	42.34	0.13	1.5	24
GEP-004	El Abra-Chuqui.	21	38.52	0.25	1.5	17	-	-	-	-
SID-16-21	El Abra-Chuqui.	29	41.70	0.79	2.5	4	42.62	0.13	1.3	22
SID-16-72	Centinela	24	62.08	0.52	1.3	10	63.75	0.47	1.6	10
SID-16-89	Centinela	16	45.13	0.36	2.0	8	45.34	0.30	1.7	11
SID-16-82	Centinela	31	51.44	0.62	0.65	15	-	-	-	-
SID-16-86	Centinela	14	51.47	0.47	1.6	12	51.81	0.50	1.8	12
SID-16-88	Centinela	30	44.03	0.43	0.37	16	-	-	-	-
SID-16-26	Centinela	13	44.55	0.39	0.68	13	-	-	-	-
SID-16-42	Escondida	25	41.88	0.42	2.0	6	42.87	0.19	1.4	14
SID-16-45	Escondida	12	43.10	0.24	1.1	6	43.59	0.37	1.7	6
SID-16-44	Escondida	32	42.97	0.13	1.4	22	43.16	0.14	1.6	20
SID-16-37	Escondida	21	68.28	0.55	0.97	19	-	-	-	-
SID-16-43	Escondida	30	43.31	0.24	1.5	21	-	-	-	-
SID-16-41	Escondida	30	66.77	0.50	1.5	18	67.25	0.44	1.5	22
SID-16-31	Escondida	36	49.43	0.16	1.6	18	49.82	0.17	1.5	19
SID-16-35	Escondida	40	48.88	0.15	1.6	22	49.22	0.15	1.4	21

Notes: - = no interpretation, MSWD = mean square of weighted deviates, n = total number of analyses, N_1 = number of dates included in the population used to calculate WM_1, N_2 = number of dates included in the population used to calculate WM_2, WM_1 = weighted mean age interpretation based on a population including the youngest date, WM_2 = weighted mean age interpretation based on a population where the oldest and youngest dates have been rejected until an acceptable MSWD has been obtained

yields a statistically acceptable MSWD (WM_1 in Table 2). This interpretation is made on the assumption that resolvable, older dates reflect geologic dispersion induced by antecrystic zircon growth and/or subtle common Pb components within the analyses. The latter biases $^{206}Pb/^{238}U$ dates toward older values. Where samples contained a dominant central population of dates with both older and younger outliers, a second evaluation was conducted by rejecting the oldest and youngest data points until a statistically acceptable MSWD was obtained (WM_2 in Table 2). This second interpretation is made on the assumption that the observed dispersion in dates is induced by the effects attributed to WM_1, in addition to a component of Pb loss in the youngest dates.

Where present, the offset between the two age interpretations in the samples is typically below 1%—too small to significantly affect the geologic interpretations. For consistency, WM_1 was chosen as the preferred age interpretation and used in the exhumation rate calculations. The preferred

emplacement age interpretations of the 49 samples range between 314.5 ± 1.7 and 35.26 ± 0.34 Ma (Table 2; Fig. 5) and define four different age groups: Carboniferous-Permian, Triassic, Late Cretaceous-Paleocene, and Eocene.

Due to limitations in the absolute accuracy of the LA-ICP-MS method of ~2% (Schaltegger et al., 2015), because data are not corrected for initial ^{230}Th disequilibrium (equating to an additional ~90 k.y. on each age interpretation), and due to the offset between age interpretations of complex U-Pb data for individual samples, we do not attempt to resolve geologic events at a temporal resolution beyond a conservative ~1 m.y., despite the uncertainties of individual statistically derived age

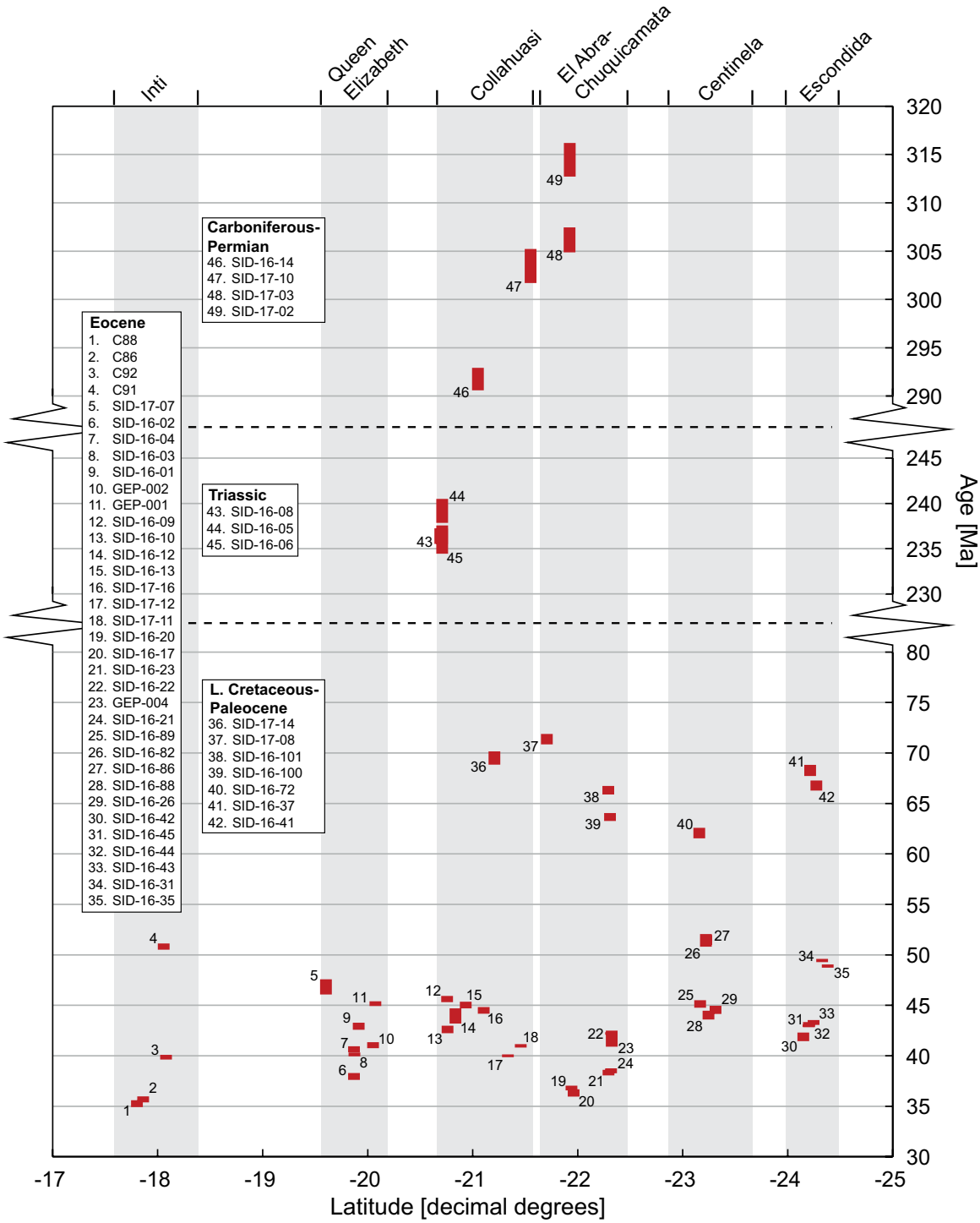

Fig. 5. Interpreted zircon laser ablation-inductively coupled plasma-mass spectrometry $^{206}Pb/^{238}U$ weighted mean emplacement ages (WM_1 in Table 2) of the intrusive rocks plotted against latitude. Note that ordinate axis is compressed between 230 and 80 Ma and 290 and 245 Ma. Error bars represent 2σ uncertainties.

calculations being discernably lower. Analytical results including beam intensities, isotope ratios, dates, and concordance for single data points are presented in Appendix 4 along with weighted mean interpretations of $^{206}Pb/^{238}U$ isotope ratios.

Al-in-Hornblende Geobarometry

Principle

The total Al content of igneous hornblende is governed by several pressure- and temperature-sensitive exchange reactions:

tremolite + phlogopite + 2 albite + 2 anorthite = 2 pargasite + 6 quartz + orthoclase; (1a)

phlogopite + 2 quartz + 2 anorthite = tschermakite + orthoclase; (1b)

tremolite + albite = edenite + 4 quartz; (1c)

edenite + albite = richterite + anorthite. (1d)

In general, those involving octahedral aluminum (Al^{VI}), such as equations (1a, b), are more pressure sensitive (Hollister et al., 1987; Johnson and Rutherford, 1989), and those involving tetrahedral aluminum (Al^{IV}) (eq. 1c, d) are more temperature sensitive (Blundy and Holland, 1990; Holland and Blundy, 1994). The Al content of amphibole is also affected by mineral assemblage, bulk composition, and oxygen fugacity (e.g., Hammarstrom and Zen, 1986; Anderson and Smith, 1995). Hammarstrom and Zen (1986) and Hollister et al. (1987) argued that for low thermodynamic variance granitic systems close to the H_2O-saturated solidus (which is roughly isothermal above 2.5 kbar), hornblende composition is dependent chiefly on pressure. This dependence is most pronounced in the total Al content ($Al^T = Al^{IV} + Al^{VI}$) leading to calibration of an Al-in-hornblende geobarometer for granitic rocks calibrated against pressure constraints from their metamorphic aureoles. Subsequent calibrations (Johnson and Rutherford, 1989; Thomas and Ernst, 1990; Schmidt, 1992; Anderson and Smith, 1995; Ridolfi et al., 2010; Ridolfi and Renzulli, 2012; Mutch et al., 2016) used amphibole data from high pressure-temperature (P-T) experiments. The different geobarometer calibrations yield variable pressures for the same amphibole composition. It is therefore important to assess which calibration provides the most accurate results for a specific problem, ideally by comparing Al-in-hornblende geobarometry pressures with an independent reliable pressure estimate.

The low thermodynamic variance approach requires that a buffering assemblage of minerals (plagioclase, hornblende, biotite, quartz, K-feldspar, magnetite, ilmenite/titanite, apatite; Mutch et al., 2016) and water-saturated melt coexist in equilibrium. However, even in the presence of the buffering assemblage, there are rival temperature and pressure controls on the Al^T content of amphiboles. Consequently, it is necessary to confirm that the amphibole compositions correspond to temperatures of the H_2O-saturated solidus. This obviates the problem of suprasolidus amphiboles being used for barometry, which will lead to overestimates of the pressure. Subsolidus alteration, on the other hand, may cause formation of low-Al amphiboles and an underestimation of pressure.

Methodology

To evaluate the available Al-in-hornblende barometer formulations, we performed a test using amphibole rim compositions from the Peach Spring tuff (USA). This tuff has the appropriate mineral assemblage, and both amphibole analyses and modeled pressures of equilibration (using rhyolite-MELTS) are available (Pamukcu et al., 2015). Rhyolite-MELTS modeling yields a preeruption storage pressure between 1.85 and 2.30 kbar. Applying the nine Al-in-hornblende barometers (Hammarstrom and Zen, 1986; Hollister et al., 1987; Johnson and Rutherford, 1989; Thomas and Ernst, 1990; Schmidt, 1992; Anderson and Smith, 1995; Ridolfi et al., 2010; Ridolfi and Renzulli, 2012; Mutch et al., 2016) to Peach Spring tuff amphibole rims yielded a pressure range of –4.2 to 8.5 kbar (App. 5). The closest match to the rhyolite-MELTS model is provided by Mutch et al. (2016), i.e., 1.66–2.51 kbar, and this formulation was preferred here.

In order to be suitable for geothermobarometry using the above approach, samples must meet the following criteria: (1) presence of hornblende with rims in immediate contact with plagioclase, (2) presence of the buffering mineral assemblage plagioclase, hornblende, biotite, quartz, K-feldspar, magnetite, ilmenite/titanite, and apatite in apparent textural equilibrium, (3) low degrees of hydrothermal alteration, (4) bulk composition between 55 and 80 wt % SiO_2, and (5) equilibration at or close to the appropriate water-saturated solidus.

Polished thin sections of each sample were examined under transmitted and reflected light in order to assess the first three criteria; the fourth was determined from the whole-rock geochemistry data. Criterion 5 was evaluated using geothermometer A of Holland and Blundy (1994) and is described further below. Scanning electron microscopy (SEM) was used to confirm the phase assemblage, and mineral microtextures were identified using backscattered electron (BSE) imagery. Energy dispersive spectrometry (EDS) element maps were made of some amphibole grains to identify potential element zoning. Major element compositions of amphibole and plagioclase were determined quantitatively by electron probe microanalysis using wavelength dispersive spectroscopy (WDS) on a Cameca SX100 at the University of Bristol with operating conditions of 20 kV, 10 nA, and 1-μm beam diameter. Coupled amphibole-plagioclase analyses were made on touching rims of grains in textural equilibrium. Amphibole mineral formulae were determined following Holland and Blundy (1994).

Results and interpretation

Twenty samples met all suitability criteria: all four Carboniferous-Permian samples, one Triassic sample, three Late Cretaceous-Paleocene samples, and 12 Eocene samples. Representative amphiboles are shown in Figure 6A-D. All but one of the suitable samples is from the four northern areas: Inti, Queen Elizabeth, Collahuasi, and El Abra-Chuquicamata. Where primary amphibole occurs in Centinela samples, many grains have been partly resorbed and have breakdown rims, demonstrating they were not in equilibrium at the conditions of magma emplacement (Fig. 6E, F). In the Escondida area, most samples lacked primary amphibole or were strongly altered, making it difficult to identify the precursor mafic minerals. Only one hornblende-bearing sample from this area

(granodiorite SID-16-31) was suitable for barometry. North of Centinela, many samples contain hornblende that has been completely replaced by actinolite ± chlorite ± magnetite and in rare cases biotite (Fig. 6G, H). In less altered samples, hornblende is preserved but commonly exhibits a patchy zoning pattern, caused by partial replacement by actinolite, evident as dark zones on BSE images (Fig. 6I) that correspond to zones low in aluminum (Fig. 6J).

Mineral chemistry: Amphibole rims in all but four samples range between magnesiohornblende and actinolite (Leake et al., 1997). Amphibole rims of Carboniferous-Permian sample SID-17-02 (Fig. 6A) from Sierra de Moreno differ from the others and classify mostly as ferrohornblende. Amphiboles with breakdown rims in Centinela samples SID-16-72 (Fig. 6E) and SID-16-88 (Fig. 6F) are also exceptions, classifying as magnesiohastingsite and edenite, respectively. Quartz gabbro sample SID-17-14, which was discarded from the barometry study because of its mafic composition (50.1 wt % SiO_2), has amphiboles ranging from edenite to magnesiohastingsite. Plagioclase rim compositions are relatively anorthite (An) poor; mean X_{An} ranges between 0.11 and 0.38 in all samples, except for the Late Cretaceous quartz gabbro (SID-17-14), which has a mean of 0.53. This compositional range is consistent with the experimental data used in the barometer calibration of Mutch et al. (2016), $An_{25–58}$. Full analytical results are presented in Appendix 6.

Pressure determination: When touching-pair amphibole-plagioclase analyses from an individual pluton are plotted in P-T space, they define a linear trend that crosscuts the solidus curves of granitoids (Fig. 7) as taken from Piwinskii and Wyllie (1970) and Holtz and Johannes (1994; parameterized by Mutch et al., 2016). Amphibole-plagioclase pairs thus equilibrated at temperatures both above and below solidus, consistent with the wide stability of amphibole in granitic magmas. A linear regression was made through the paired analyses; the intercept between the regression and the relevant solidus is then taken to approximate the emplacement pressure. To account for uncertainties, a cloud of 1,000 randomly distributed points was generated around each paired analysis according to the uncertainties on the barometer (±16%) and thermometer (±35°C). One thousand linear regressions were then drawn through the point clouds, and the emplacement pressure and its standard deviation were determined as the mean and standard deviation of the intercepts between the regression lines and the appropriate solidus. The effect of the analytical uncertainty (around 1% Al^T) on the final pressure estimate is insignificant compared to that from the barometer and thermometer calibrations. Even though amphibole-plagioclase analyses from samples containing only subsolidus temperatures can show a linear trend in P-T space, calculated emplacement pressures are not considered reliable unless the sample contains analyses that yield near-solidus temperatures.

Emplacement pressures and depths

Pressures obtained from the 20 suitable samples are similar regardless of age and location and lie between 1.16 ± 0.10 and 1.87 ± 0.15 kbar, except at Sierra de Moreno, where Carboniferous granodiorite SID-17-02 has a significantly higher emplacement pressure of 3.20 ± 0.28 kbar (Table 3). Pluton emplacement depths were calculated assuming a uniform upper crustal density in the Precordillera of ~2,700 kg/m^3 (Götze and Kirchner, 1997; Lucassen et al., 2001; Prezzi et al., 2009). Potential lateral density variations are ignored, and it is also assumed that the pressure experienced by a crystallizing pluton is entirely lithostatic. The emplacement depth corresponding to the calculated pressure for sample SID-17-02 is 12.1 ± 1.1 km and between 4.43 ± 0.67 and 7.05 ± 0.58 km for all other plutons (Fig. 8).

Pluton Exhumation Histories

The emplacement age and depth of 20 plutonic rocks have been precisely constrained by geochronology and geobarometry. With the exception of the two Inti drill core samples, all plutons are exposed at the surface today, so the average exhumation rate from emplacement to the present can be calculated by simply dividing emplacement depth by emplacement age. In many locations exhumation histories can be further refined by dated cover rocks, which provide minimum exposure ages for the plutons. Similarly, dated supergene minerals that formed within associated porphyry Cu deposits can constrain when they reached near-surface levels. However, caution must be taken since formation of supergene alunite can take place over considerable depth ranges (Alpers and Brimhall, 1988). For example, Chuquicamata hosts supergene alunite veins to depths of 1,000 m along high-permeability pathways created by faults (Sillitoe and McKee, 1996). Only alunite or jarosite that formed in the leached cap at the top of the weathering profile of a porphyry Cu deposit are therefore considered as reliable minimum exposure constraints. Leached caps in the Central Andes are typically a few tens to 200 m thick but reach 500 m at Escondida and El Salvador (Sillitoe, 2005, and references therein). This introduces an uncertainty in the depth the minimum exposure age

Fig. 6. Representative amphibole grains. A. Hornblende showing normal core-rim zoning in Carboniferous granodiorite SID-17-02 (Sierra de Moreno). B. Twinned hornblende crystal in Permian granodiorite SID-16-14 (Collhuasi area). C. Hornblende replacing clinopyroxene in granodiorite C91 (Inti area). D. Euhedral hornblende crystal partly replaced by pale-green actinolite in SID-16-20, Clara granodiorite (Pajonal-El Abra pluton). E. Magnesiohastinsite antecryst/xenocryst with breakdown rim rich in magnetite, actinolite, and chlorite in Late Cretaceous quartz monzonite SID-16-72 (Centinela area). F. Resorbed edenite antecryst/xenocryst in quartz monzodiorite SID-16-88 (Centinela area), with a similar breakdown rim as in E. G. Hornblende completely replaced by actinolite, biotite, and magnetite in Triassic granite SID-16-05 (Collahuasi area). H. Hornblende completely replaced by actinolite in quartz monzonite SID-16-12 (Collahuasi area). I. Backscattered electron (BSE) image of hornblende exhibiting irregular patchy zoning in SID-16-03 (Alantaya pluton). J. Aluminum X-ray map of the hornblende shown in I. Red areas are Al rich, black areas Al poor. Al-rich areas correlate with the light-colored zones in the BSE image. Mineral abbreviations: Act = actinolite, Ap = apatite, Bt = biotite, Cpx = clinopyroxene, Ed = edenite, Ep = epidote, Hbl = hornblende, Kfs = alkali feldspar, Mag = magnetite, Mhs = magnesiohastingsite, Pl = plagioclase, Qz = quartz.

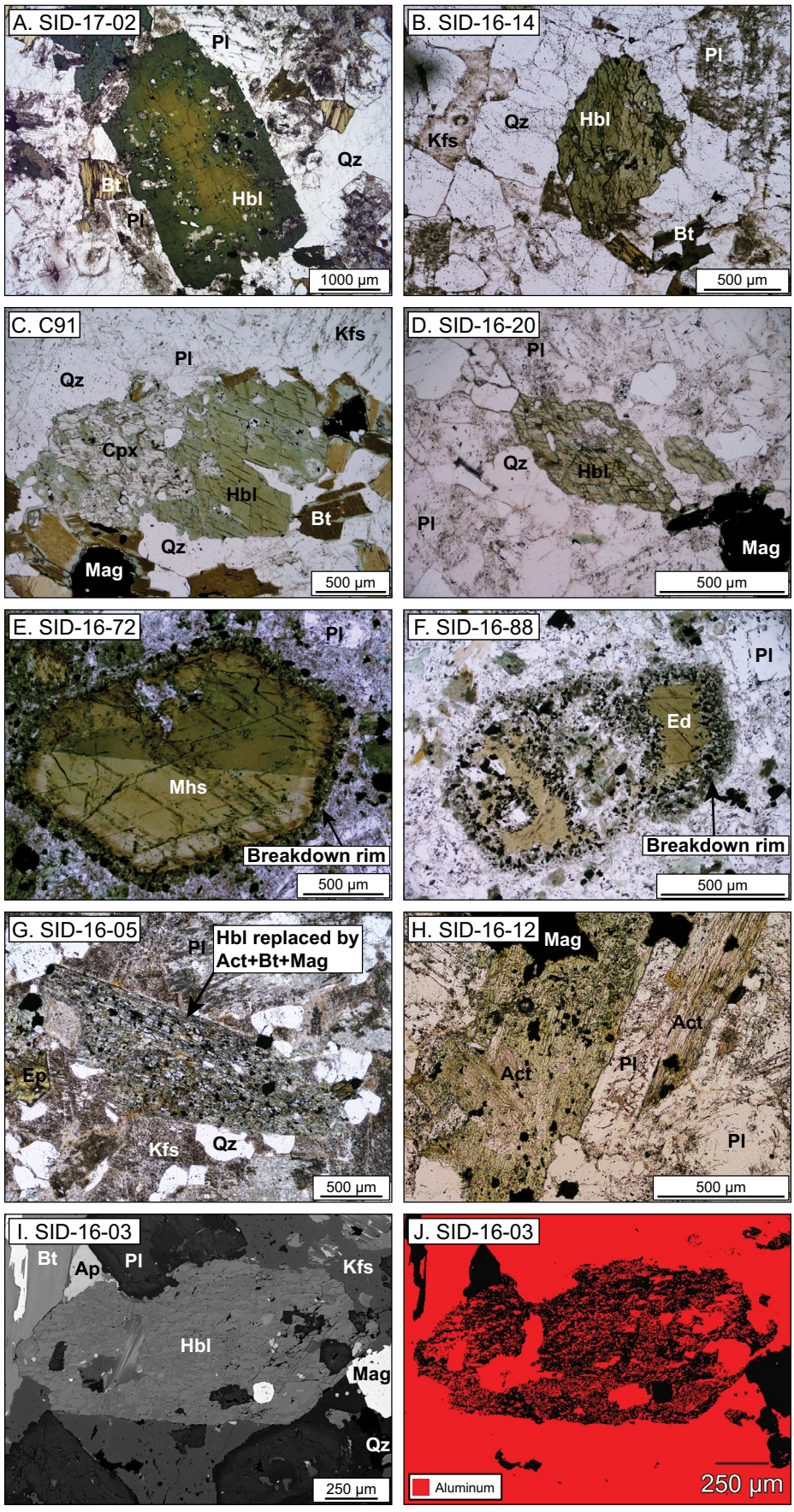

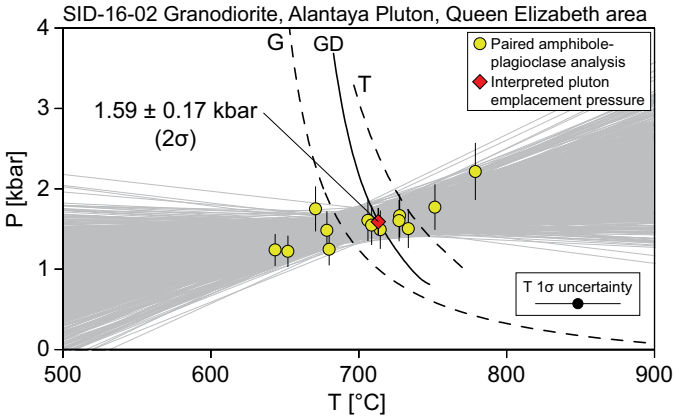

Fig. 7. Method for determining emplacement pressure. Paired amphibole-plagioclase analyses (yellow circles) are plotted in pressure-temperature (P-T) space, where P is determined with the Mutch et al. (2016) Al-in-hornblende geobarometer and T with the amphibole-plagioclase geothermometer A of Holland and Blundy (1994). Solidus curves for haplogranite (G; Holtz and Johannes, 1994 parameterized by Mutch et al., 2016), granodiorite (GD; Piwinskii and Wyllie, 1970), and tonalite (T; Piwinskii and Wyllie, 1970) are also plotted. The emplacement pressure of the sample (in this case SID-16-02) is determined as the intersection (red diamond) of the trend of points and the most appropriate (in this case GD) solidus. The gray lines illustrate the statistical method for obtaining uncertainties, as described in the text. Error bars on the paired analyses are given at the 1σ confidence level. Uncertainty on the final P estimate is given at the 2σ level.

captures. Likewise, in cases where a sample location is some distance away from the relevant cover unit, some exhumation may have happened at the sample location after the cover was deposited. However, these effects are considered to be minor and are not accounted for in the exhumation rate calculations unless stated.

For each pluton with a determined emplacement age (t_{Emp}) and depth (z_{Emp}), a minimum exposure age has been determined by the oldest dated cover unit or nearby supergene age. The average exhumation rate (R_E) is then calculated for each pluton (illustrated in Fig. 9):

$$R_E = z_{Emp}/(t_{Emp} - t_{Exp}). \quad (2)$$

Uncertainty on R_E is calculated by full error propagation. The results provide information on the timing of periods of net exhumation along the Precordillera as well as average exhumation rates during these periods at each sampled location.

Minimum exposure ages

Fifteen minimum exposure ages were estimated from dated cover units and four from dated supergene minerals (Table 3; Fig. 10). Sixteen plutons were found to have been exposed by the late Oligocene-Miocene, while three Carboniferous-Permian plutons were exposed in the Triassic-Jurassic. Only one pluton lacks cover or supergene ages that can be used to determine a minimum exposure age. All plutons are assumed to have reached the surface by the time of their minimum exposure age, apart from Queen Elizabeth samples SID-16-02 and SID-16-03, which require further explanation. These samples were taken from the floor of a valley approximately 300 m below the contact with the 25.7 ± 1.0 Ma Utayane Formation (biotite K-Ar age; Muñoz, 1991, as cited in Sellés et al., 2016), which is the oldest dated cover unit in the area and was deposited on a pediplain surface following the Incaic orogenic event (Morandé et al., 2015). For this reason, exhumation rates for samples SID-16-02 and SID-16-03 are calculated assuming that they were 300 m below the surface at 25.7 ± 1.0 Ma. Subsequently, the area has experienced continued deformation, uplift, and erosion (Morandé et al., 2015; Tomlinson et al., 2015; Sellés et al., 2016). A 12.9 ± 0.6 Ma volcanic deposit (whole-rock K-Ar age; Baker and Francis, 1978) sourced from the Cerro Patara volcano reaches the valley floor, suggesting that the final ~300 m plus the cover thickness must have eroded by this time, exposing the samples. See Appendix 7 for a detailed justification of all exposure ages.

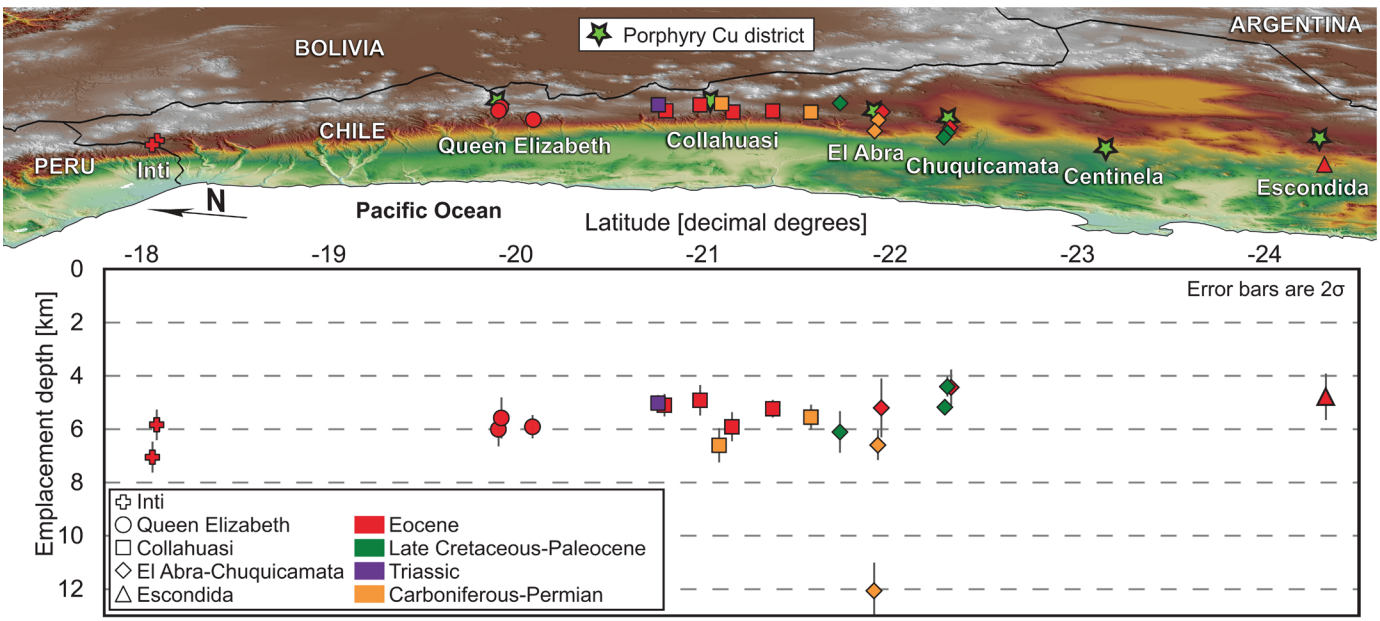

Fig. 8. Oblique view of northern Chile showing sample locations along the Precordillera and corresponding pluton emplacement depths. Emplacement depths range between ~4 and ~7 km, except for sample SID-17-02, at 12.1 ± 1.1 km.

Table 3. Emplacement Ages, Pressures, Depths, Minimum Exposure Ages, and Average Exhumation Rates of Plutonic Rocks

	Zircon U-Pb		Al-in-hornblende				Minimum exposure ages				Exhumation rates	
Sample	Age (Ma)	2σ (Ma)	P (kbar)	2σ (kbar)	Depth (km)	2σ (km)	Age (Ma)	2σ (Ma)	Constraint unit	Age reference	Average (km/m.y.)	2σ (km/m.y.)
SID-17-02	314.5	1.7	3.20	0.28	12.1	1.1	166.9	3.4	Quehuita Formation[1]	Skarmeta (1983)	0.082	0.007
SID-17-03	306.2	1.3	1.75	0.15	6.60	0.56	179.55	11.25	Quehuita Formation[1]	Ardill et al. (1998), Gröschke and Wilke (1986)	0.052	0.006
SID-17-10	303.5	1.8	1.47	0.12	5.54	0.47	43.3	1.6	Sichal Formation	Tomlinson et al. (2001)	0.021	0.002
SID-16-14	291.8	1.2	1.75	0.17	6.60	0.64	239	7	Strata of Quebrada Conacona[2]	Tomlinson et al. (2001)	0.125	0.021
SID-16-06	236.0	1.6	1.33	0.08	5.02	0.30	16.6	1.1	Huasco ignimbrite	Tomlinson et al. (2001)	0.023	0.001
SID-16-100	63.60	0.41	1.16	0.10	4.40	0.38	20.8	1.2	Ministro Hales supergene	Sillitoe and McKee (1996)	0.103	0.009
SID-16-101	66.31	0.42	1.37	0.07	5.17	0.26	20.8	1.2	Ministro Hales supergene	Sillitoe and McKee (1996)	0.114	0.007
SID-17-08	71.38	0.51	1.62	0.21	6.10	0.78	5.8	0.4	Carcote ignimbrite	Tomlinson et al. (2001)	0.093	0.012
C92	50.82	0.32	1.87	0.15	7.05	0.58	21.947	0.017	Oxaya Fm. (Cardones ign.)	van Zalinge et al. (2016)	0.244	0.020
C91	39.86	0.24	1.55	0.15	5.84	0.57	21.947	0.017	Oxaya Fm. (Cardones ign.)	van Zalinge et al. (2016)	0.326	0.032
SID-16-02	40.65	0.30	1.59	0.17	6.00	0.64	25.7	1.0	Utayane Formation	Muñoz (1991), as cited in Sellés et al. (2016)	0.381[3]	0.049
SID-16-03	40.14	0.19	1.48	0.20	5.58	0.77	25.7	1.0	Utayane Formation	Muñoz (1991), as cited in Sellés et al. (2016)	0.366[3]	0.057
GEP-002	41.05	0.30	1.56	0.12	5.91	0.44	19.59	0.27	Altos de Pica Fm. (Tambillo ign.)[4]	Gardeweg and Sellés (2013)	0.275	0.021
SID-16-09	45.61	0.31	1.35	0.11	5.10	0.42	16.6	1.1	Huasco ignimbrite	Tomlinson et al. (2001)	0.176	0.016
SID-16-13	45.03	0.33	1.30	0.15	4.92	0.57	16.6	1.1	Huasco ignimbrite	Tomlinson et al. (2001)	0.173	0.021
SID-17-16	44.49	0.34	1.57	0.14	5.91	0.54	5.8	0.4	Carcote ignimbrite	Tomlinson et al. (2001)	0.153	0.014
SID-17-12	40.00	0.13	1.39	0.09	5.23	0.33	24.75	1.65	Papajoy Formation[5]	Tomlinson et al. (2001)	0.343	0.043
SID-16-20	36.80	0.24	1.38	0.29	5.20	1.10	13.10	0.20	Conchi supergene	Perelló (2003)	0.219	0.047
SID-16-21	42.21	0.12	1.17	0.18	4.43	0.67	20.8	1.2	Ministro Hales supergene	Sillitoe and McKee (1996)	0.207	0.033
SID-16-31	49.43	0.16	1.27	0.23	4.78	0.87	0	0	-	-	0.097	0.018

- = no constraint unit exists

[1]Ages of the Quehuita Formation are based on the fossil record in the units closest to each sample location and on sequence stratigraphy in Ardill et al. (1998)

[2]The age used is considered a minimum age for the unit, obtained from the intruded Loa Porphyry

[3]Calculated from the emplacement depth to 300 m below the surface, given by the likely depth of the sample lcoation at the time of cover deposition

[4]The age used is for the Tambillo ignimbrite, which is intercalated with the Altos de Pica Formation near the sample location

[5]The age used is based on a range of ages of intercalated tuff layers in the Papajoy Formation

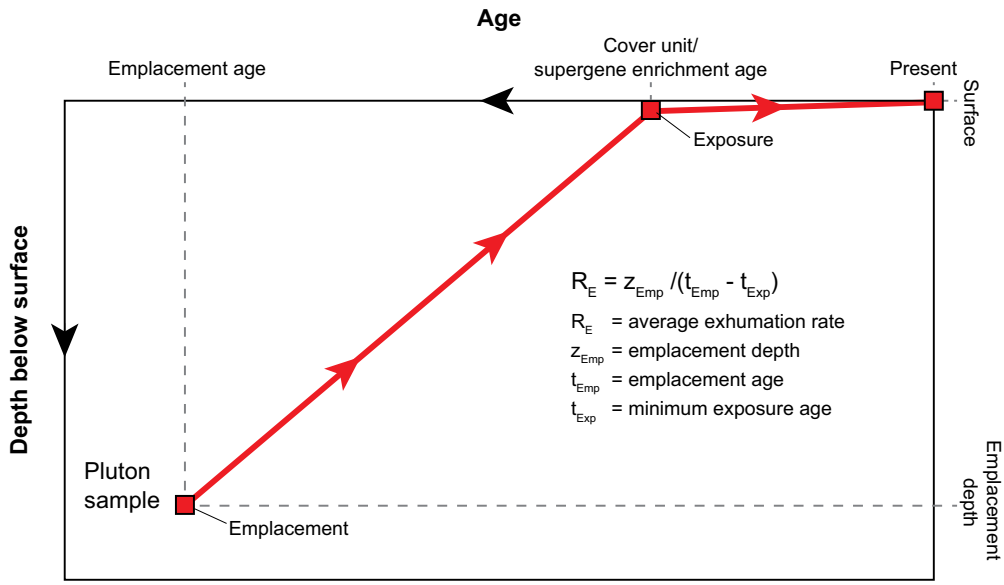

Fig. 9. Schematic representation of how the average pluton exhumation rate is calculated. Pluton emplacement ages and depths are determined by U-Pb geochronology and Al-in-hornblende geobarometry, respectively. Minimum exposure ages are constrained by dated cover units or ages of supergene minerals formed in leached caps of porphyry Cu deposits in the vicinity of the sampled plutons. Average exhumation rate is calculated as the emplacement depth divided by the time between emplacement and surface exposure or arrival within a few hundred meters of the surface. Minor exhumation may in some cases have taken place after the age of exposure, as cover units rarely cover the immediate sample location, and leached caps of porphyry Cu deposits may reach thicknesses up to a few hundred meters.

Exhumation rates

The timings and average rates of pluton exhumation throughout the study area are presented in Figure 11. Average rates for the Carboniferous-Permian plutons range from 0.018 ± 0.002 to 0.125 ± 0.021 km/m.y., with the highest for sample SID-16-14 from the Collahuasi area, which had been exposed by the Triassic. The Triassic-Paleocene plutons range between 0.023 ± 0.001 and 0.113 ± 0.007 km/m.y., though none showed evidence of pre-Miocene surface exposure. For the Eocene plutons, average exhumation rates range between 0.097 ± 0.018 and 0.381 ± 0.049 km/m.y., and exhumation is generally bracketed between the late Eocene and late Oligocene-middle Miocene. The highest exhumation rates are recorded in the Queen Elizabeth area where there is only ~15 m.y. between emplacement and near-surface arrival. Samples SID-16-02 and SID-16-03 experienced an additional pulse of at least 300 m of exhumation between deposition of the oldest cover unit (at 25.7 ± 1.0 Ma) and final surface exposure (by 12.9 ± 0.6 Ma) at a minimum average rate of ~0.023 km/m.y.

Discussion

Pluton emplacement ages

The emplacement ages determined in this study are generally consistent with previously published ages with three notable exceptions: one sample of granodiorite from the Longacho pluton (SID-16-05) and two samples from the Caballuno pluton (granite SID-16-06 and mineralized feldspar porphyry SID-16-08) in the Collahuasi area (Fig. 1B) yielded Triassic ages rather than the expected Eocene ages (Longacho: 45.3 ± 0.4 Ma; Caballuno: 45.7 ± 4.6 Ma; Vergara and Thomas, 1984). This apparent discrepancy is probably due to the presence of texturally and compositionally similar Triassic and Eocene phases in these bodies, as noted elsewhere along the Precordillera (Zentilli et al., 2018). Overall, Eocene plutons in the Collahuasi, Centinela, and Escondida areas are older than those in the Inti, Queen Elizabeth, and El Abra-Chuquicamata areas.

Pluton emplacement depths

The consistency of pluton emplacement at epizonal depths of ~4–7 km, regardless of age, suggests an intrinsic physical control. Magmas can stall at a specific crustal depth for a number of reasons, such as magma viscosity, buoyancy, local stress regime, and crustal architecture (Chaussard and Amelung, 2014, and references therein). Annen et al. (2006) introduced the concept of "viscous death," whereby buoyant hydrous magmas ascend through the crust until reaching their H_2O-saturated liquidus, whereupon H_2O exsolves and crystallization starts. Both fluid exsolution and crystallization increase the viscosity of the magma, which inhibits further ascent. In this model, the depth at which a magma crystallizes is primarily controlled by its H_2O content. A wet magma would stall at a deeper level than a dry magma. If viscous death is the primary control on pluton emplacement depth in the study area, it follows that all plutons with similar emplacement depths had similar magmatic H_2O contents. It is possible that the plutons in the Centinela and, in particular, Escondida areas with relatively dry clinopyroxene-rich mineralogies stalled at shallower levels than the amphibole-biotite–rich plutons farther north. Hornblende breakdown is commonly observed in volcanic rocks that have equilibrated at pressures below the minimum stability of this mineral (~1 kbar for dacite magmas; Rutherford and Hill, 1993).

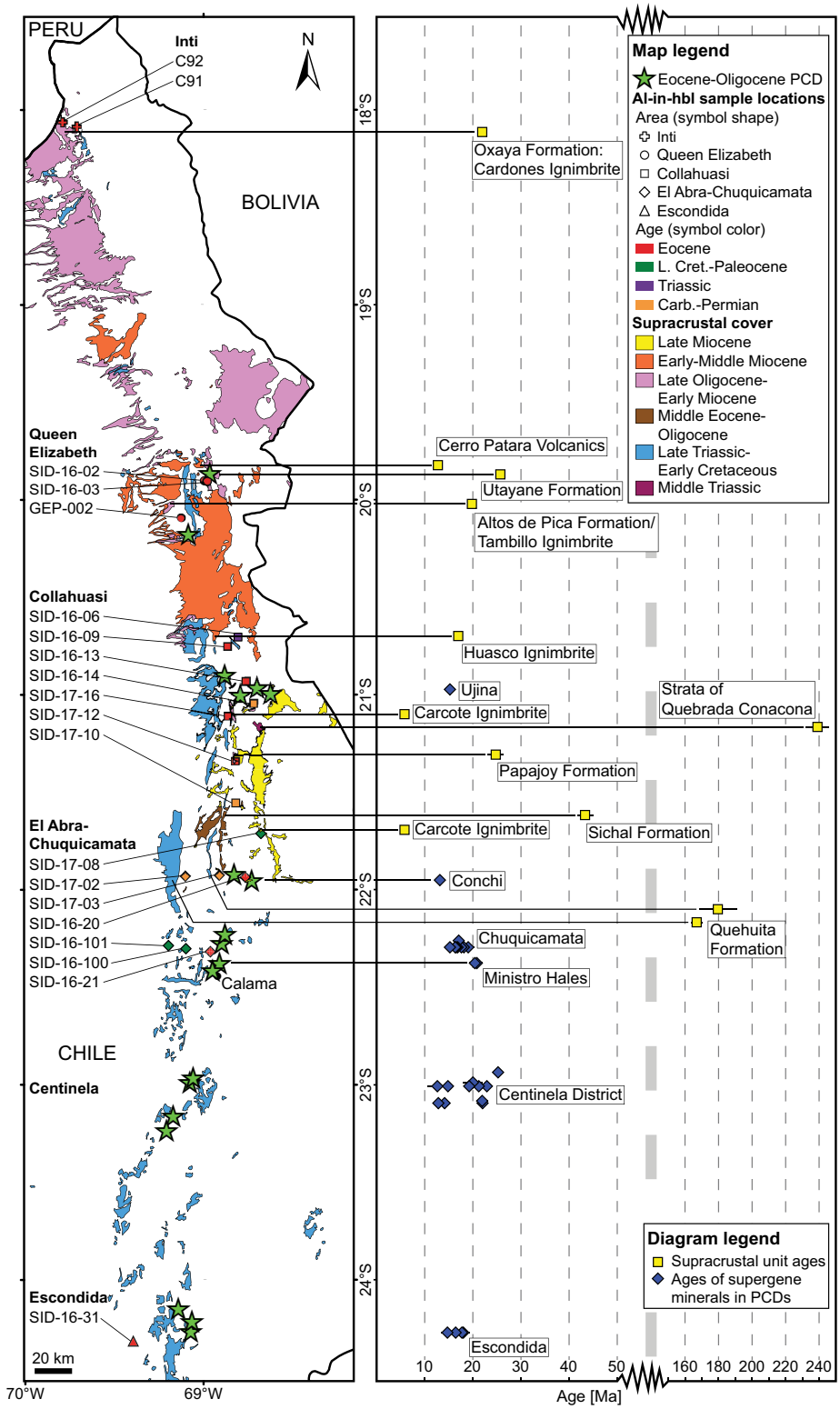

Fig. 10. Distribution of supracrustal cover units used to constrain minimum exposure ages. Ages of the cover units (Table 3) are shown along with ages of supergene minerals in porphyry Cu deposits, which in two locations (Ministro Hales and Conchi) have also been used as approximate minimum exposure ages of nearby plutons. Note the break in the age axis between 150 and 50 Ma and the different scales on either side of the break. Cover units are modified after SERNAGEOMIN (2003) and Morandé et al. (2015), locations of porphyry Cu deposits after Tomlinson et al. (2001), Singer et al. (2008), and Mpodozis and Cornejo (2012). Ages of supergene minerals compiled from Alpers and Brimhall (1988), Sillitoe and McKee (1996), Mote et al. (2001), Perelló (2003), and Riquelme et al. (2017). Abbreviations: Carb. = Carboniferous, hbl = hornblende, L. Cret. = Late Cretaceous, PCD = porphyry copper deposit.

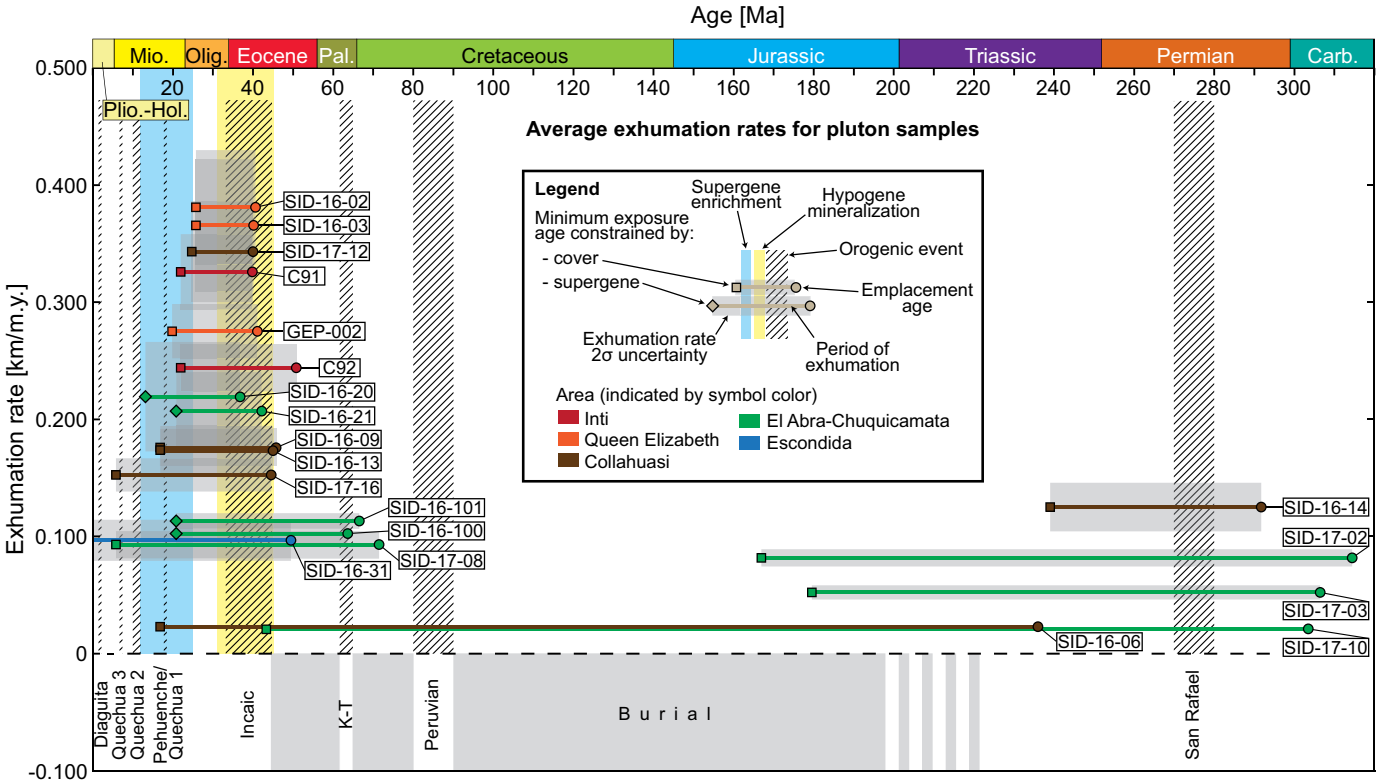

Fig. 11. Timings and average rates of exhumation of pluton samples. The data delineate two periods of net exhumation between the Carboniferous-Permian and Triassic-Jurassic, and between the Eocene and late Oligocene-early Miocene, possibly correlated with the San Rafael and Incaic orogenic events, respectively. The period between the Late Triassic and Eocene was probably a period of net burial in most parts of the Precordillera. The highest exhumation rates (~0.40 km/m.y.) are recorded in the Queen Elizabeth area, where the ~40 Ma northeastern part of the Alantaya pluton was covered by ~25 Ma volcanic rocks of the Utayane Formation. Timing of orogenic events are compiled from Llambías and Sato (1990), Scheuber et al. (1994), Kay et al. (1999), Tomlinson et al. (2001), Cornejo et al. (2003), and Mpodozis and Cornejo (2012). Timing of hypogene mineralization (Sillitoe and Perelló, 2005; Mpodozis and Cornejo, 2012) and supergene enrichment (Alpers and Brimhall, 1988; Sillitoe and McKee, 1996; Mote et al., 2001; Perelló, 2003; Riquelme et al., 2017) are shown for middle Eocene-early Oligocene porphyry Cu deposits within the study area. Abbreviations: Carb. = Carboniferous, Hol. = Holocene, Mio. = Miocene, Olig. = Oligocene, Pal. = Paleocene, Plio. = Plicoene.

The only exception to epizonal emplacement within the study area is the 12.1 ± 1.1-km-deep Carboniferous pluton at Sierra de Moreno (SID-17-02). The greater depth is supported by the geologic context: in contrast to the Carboniferous-Permian plutons of Cerro Jaspe and Sierra del Medio farther east, which intruded a thick package of approximately coeval volcanic and sedimentary rocks, the pluton at Sierra de Moreno intruded early Paleozoic metamorphic rocks (Damm et al., 1990; Tomlinson et al., 2001; Loewy et al., 2004). These metamorphic rocks represent a lower structural level, inferred to be part of the basement onto which the Carboniferous-Triassic surface units were deposited (Tomlinson et al., 2001; Tomlinson and Blanco, 2008).

Temporal exhumation patterns

The ages and exhumation rates determined in this study delineate two regionally important periods of exhumation: early Permian to Middle Triassic and middle Eocene to late Oligocene.

The fact that several Carboniferous-Permian plutons exposed at the surface by the Late Triassic or Jurassic are preserved alongside Eocene plutons with 4–7 km of postemplacement exhumation requires a period of net burial that returned the Carboniferous-Permian plutons to depths of 4–7 km prior to Eocene emplacement. This burial could have been accomplished by the abundant supracrustal rocks deposited across northern Chile during regional extension between the Late Triassic and middle Eocene (Cornejo et al., 2003; Charrier et al., 2007; Armijo et al., 2015). Jurassic-Early Cretaceous sediments deposited in the back-arc basin that developed in the Central depression and Precordillera probably reached thicknesses of at least 10 km in places (Armijo et al., 2015, and references therein). Several Late Cretaceous-middle Eocene volcano-sedimentary units, such as Tolar, Cerro Empexa, Quebrada Mala, Augusta Victoria, and Icanche, were subsequently deposited in continental basins along the Precordillera (Charrier et al., 2007). The extensional regime was interrupted by relatively short-lived compressional events, most notably the ~90–80 Ma Peruvian (Scheuber et al., 1994) and the ~65–62 Ma K-T (Cornejo et al., 2003) orogenic events, which caused deformation and depositional hiatuses (Tomlinson et al., 2001, 2015; Morandé et al., 2015; Sellés et al., 2016). Although some exhumation probably occurred during these events, it is unlikely to have been enough to counteract the overall net burial.

The Eocene plutons were all exhumed from depths of 4–7 km and, in several locations, show evidence of exposure by the late Oligocene-early Miocene. Average exhumation rates in several places exceed 0.30 km/m.y., although they are likely to encompass periods of faster and slower exhumation. For example, faster exhumation could have taken place at an early stage, correlated with the ~45–33 Ma Incaic orogenic event (Tomlinson et al., 2001; Mpodozis and Cornejo, 2012), in agreement with thermochronometric studies by Maksaev and Zentilli (1999) and Sanchez et al. (2018), who proposed slower rates after the early Oligocene (<~0.05 and <~0.09 km/m.y., respectively). Pre-Eocene and Eocene plutons likely experienced contemporaneous exhumation, which is supported by Eocene AFT ages of Carboniferous-Triassic plutons in Sierra del Medio (Maksaev and Zentilli, 1999), indicating residence beneath the AFT partial annealing zone until this time. Most AHe ages obtained in the study area fall between the middle Eocene and late Oligocene (Stalder et al., 2020, and references therein), underpinning that rocks exposed at the surface today were at shallow crustal depths already at this time (AHe closure happens at depths <~2.5 km, assuming a closure temperature of ~70°C, Farley, 2000; and a geothermal gradient of ~30°C/km, Maksaev and Zentilli, 1999).

Early Miocene and later exhumation rates in the Precordillera must have been relatively low, since rocks exposed at this time are still preserved at the surface today. Slow exhumation is consistent with an increasingly dry climate since the early Miocene (Dunai et al., 2005; Evenstar et al., 2009, 2017; Rech et al., 2019), the formation of regionally extensive late Oligocene-late Miocene geomorphic surfaces, often interpreted as pediplains (Galli-Olivier, 1967; Mortimer, 1973; Dunai et al., 2005; Kober et al., 2007; Bissig and Riquelme, 2009; Evenstar et al., 2017; Riquelme et al., 2017) and low erosion rates (<0.01 km/m.y.) calculated from cosmogenic surface exposure dating (Dunai et al., 2005; Kober et al., 2007; Evenstar et al., 2009, 2017).

Spatial exhumation patterns

Early Permian-Early Jurassic: Constraints on pre-Eocene exhumation are confined to the center of the study area where older plutons are exposed within different crustal blocks. The apparent variation in exhumation rate between Carboniferous-Permian samples SID-16-14 from Sierra del Medio, SID-17-03 from Cerro Jaspe, and SID-17-10 from Cordon del Millo (Fig. 1A), between 0.021 ± 0.002 and 0.125 ± 0.021 km/m.y., is due to differences in cover unit ages that constrain their time of exposure (Fig. 11). It is possible that the differences are real, but the plutons could instead have been exhumed simultaneously at the same rate and then been covered diachronously. Another possibility is that cover units are not preserved in every location. Sample SID-17-02 from Sierra de Moreno must have had a different exhumation history than the other Carboniferous-Permian samples for a much deeper crustal level to have been exposed by the Jurassic. Higher exhumation rates at SID-17-02 are supported by the amphibolite-granulite facies metamorphic rocks exposed in this location (Damm et al., 1990; Tomlinson et al., 2001; Loewy et al., 2004) and by the variability in exhumed thicknesses between crustal blocks during the Permian San Rafael orogenic event (Tomlinson et al., 2001, 2012; Tomlinson and Blanco, 2008).

Middle Eocene-late Oligocene: Average exhumation rates for Eocene plutons during this period were ~0.30–0.40 km/m.y., and the total amount of exhumation was ~5–6 km. As with the older intrusions, spatial variations in exhumation rate are possibly a function of the pluton and minimum exposure ages bracketing the period of exhumation. In reality, all locations may have experienced a period with an average exhumation rate >0.30 km/m.y. between the late middle Eocene and early Oligocene, which is only captured where a suitable late middle Eocene pluton and a late Oligocene lower bracket are available. Nevertheless, local variations are suggested by differences in the ages of exposed plutons. For example, near El Abra, sample SID-16-20 was emplaced at 36.8 ± 0.2 Ma and 5.20 ± 1.10-km depth, whereas Collahuasi samples SID-16-09 and SID-16-13 were emplaced at similar depths of 5.10 ± 0.42 and 4.92 ± 0.57 km, respectively, but are substantially older (45.61 ± 0.31 and 45.03 ± 0.33 Ma, respectively). Magmatism at Collahuasi continued until at least ~34 Ma, as indicated by the age of the Rosario porphyry Cu deposit (Masterman et al., 2004), but the apparent lack of exposed plutons <40 Ma may indicate that the deep plutonic environment of this age has not yet reached the surface. Masterman et al. (2005) estimated ~1 km of erosion in ≤2 m.y. during formation of the Rosario deposit, suggesting that at least one pulse of relatively fast exhumation has occurred in the Collahuasi district, but the total exhumed thickness since the late Eocene was probably less than at El Abra. Likewise, the abundance of potentially shallow, clinopyroxene-dominated plutons at Centinela and Escondida suggests relatively limited exhumation.

Early Miocene-Present: From the early Miocene onward, exhumation rates across the Precordillera were consistently low but appear to have been slightly higher north of ~20°S, as indicated by the evidence for deformation, uplift, and erosion in the Queen Elizabeth area between the late Oligocene and middle Miocene (Morandé et al., 2015; Tomlinson et al., 2015; Sellés et al., 2016).

Summary and interpretation

Based on the Eocene and later pluton exhumation histories and other geologic constraints discussed above, it is possible to divide our studied section of the Precordillera into three segments: a northern segment comprising areas north of and including Queen Elizabeth, a central segment between and including Collahuasi and El Abra-Chuquicamata, and a southern segment comprising Centinela and Escondida (Fig. 12A). The northern segment experienced relatively fast exhumation throughout the Eocene-late Oligocene, was covered to a greater extent than areas farther south by thick late Oligocene-early Miocene volcanic deposits, and shows evidence of greater post-early Miocene deformation and exhumation. The central segment records slower exhumation, even though relatively young and deeply emplaced plutons are locally exposed (e.g., El Abra). The southern segment comprises abundant fine-grained, clinopyroxene-bearing (rather than amphibole-bearing) plutons, which may indicate shallow emplacement depths and less post-Eocene exhumation than in the northern and central segments.

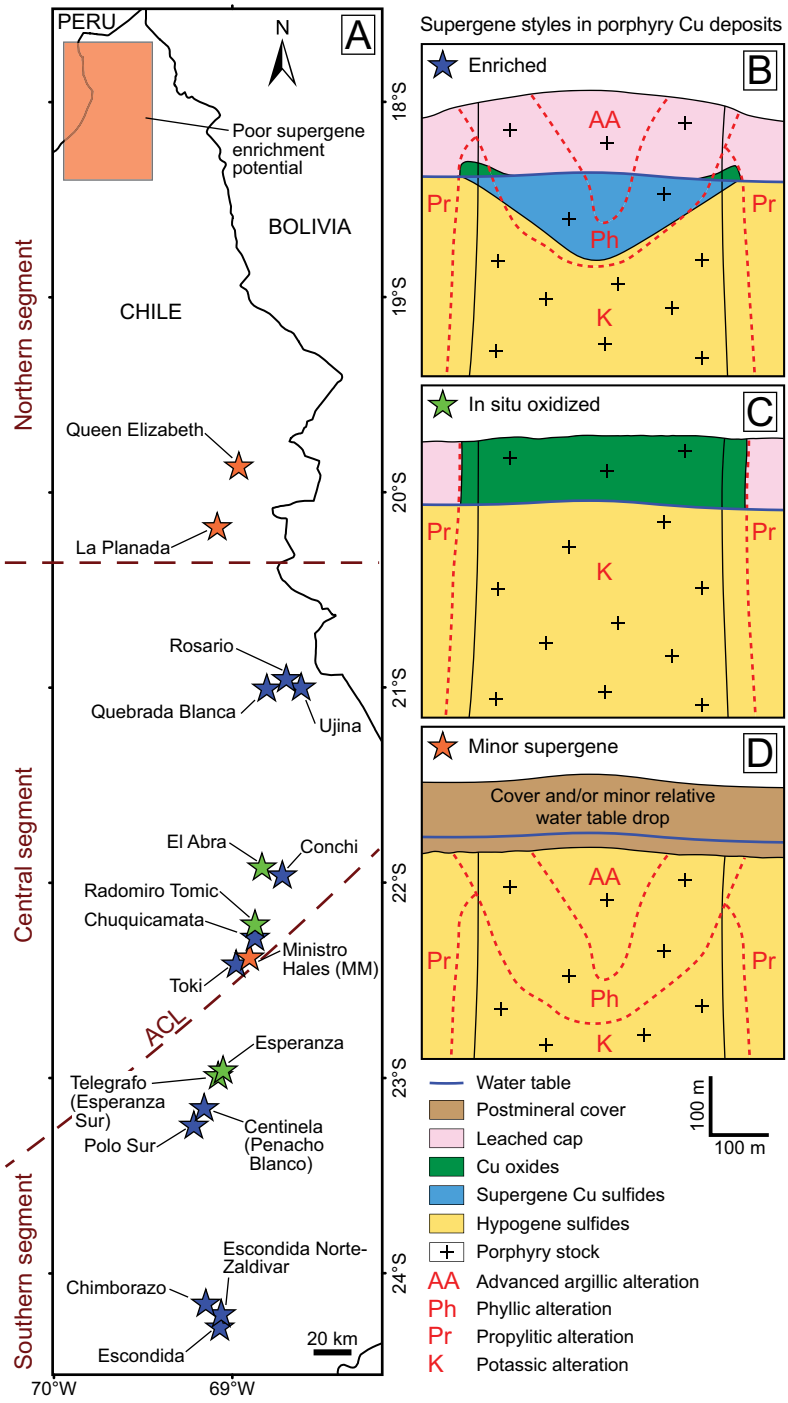

Fig. 12. A. Map showing the locations of segments outlined in the text and distribution of middle Eocene-early Oligocene porphyry Cu deposits displaying the different supergene styles shown in schematic cross sections B, C, and D. Porphyry Cu deposits classified using descriptions in Ambrus (1977), Dick et al. (1993), Bisso et al. (1998), Cuadra and Camus (1998), Sillitoe et al. (1998), Ossandón et al. (2001), Padilla Garza et al. (2001), Camus (2003), Perelló (2003), Perelló et al. (2004, 2010), Sillitoe (2005), Rivera et al. (2009), and Hervé et al. (2012). ACL = Antofagasta-Calama lineament.

The boundary between the northern and central segments is located at a dividing line between late Oligocene-early Miocene cover rocks that largely overlap with the axis of the Eocene-Oligocene arc to the north, and younger cover rocks mostly located east of the Eocene-Oligocene arc to the south (Freymuth et al., 2015). Early-middle Miocene flat-slab subduction south of ~20°S has been suggested as the explanation for the lack of volcanic rocks of this age in this area (e.g., Wörner et al., 2000; Ramos and Folguera, 2009). The northern segment comprises a series of N-trending anticlines, formed by mainly Oligocene-Miocene deformation, which has led to uplift and erosion (Farías et al., 2005; Sellés et al.,

2016; van Zalinge et al., 2017). The Queen Elizabeth area is located in the core of one of the anticlines (Sellés et al., 2016), which may partly explain its relatively high exhumation rates during this time.

The boundary between the central and southern segments coincides with the Antofagasta-Calama lineament, a fault zone that initiated in the Eocene and has been interpreted as the boundary between two basement terranes—Antofalla to the north and Chilenia to the south—based on different paleomagnetic rotation patterns and isotope signatures (Arriagada, 2018; Bunker, 2020). It is likely that the different rotation patterns reflect differing histories of deformation and thus exhumation either side of the fault zone.

Implications for Porphyry Cu Formation

Our study suggests that within the Precordillera of northern Chile, periods of exhumation in the early Permian-Middle Triassic and Eocene-late Oligocene, separated by a Late Triassic-middle Eocene period of net burial, led to preservation at near-surface levels of epizonal rocks from time periods spanning ca. 300 m.y. Consequently, a belt of subeconomic Permian-Triassic porphyry Cu deposits, which formed prior to the phase of net burial, is preserved alongside major porphyry Cu deposits of the superimposed middle Eocene-early Oligocene metallogenic belt (Cornejo et al., 2019). The Permian-Triassic porphyry Cu deposits have characteristics similar to those of their younger counterparts but lack economic metal endowments (Cornejo et al., 2019).

Patterns of post-Eocene exhumation must have been conducive for the formation, enrichment, and preservation of the middle Eocene-early Oligocene porphyry Cu deposits, as previously suggested by Maksaev and Zentilli (1999) and Sanchez et al. (2018). Hypogene ore formation benefited from relatively high exhumation rates, resulting in large, high-grade orebodies, of which several were telescoped and enhanced by a late-stage high-sulfidation overprint, e.g., Chuquicamata (Ossandón et al., 2001), Escondida (Padilla Garza et al., 2001; Hervé et al., 2012), Escondida Norte-Zaldivar (Hervé et al., 2012), Rosario (Masterman et al., 2005), and Ministro Hales (Sillitoe et al., 1998; Boric et al., 2009). The subsequent slowing of exhumation from the late Oligocene-early Miocene onward created ideal conditions in many locations for supergene enrichment and surface preservation of the orebodies (Sillitoe, 2005). However, the belt also includes several poorly enriched deposits that were either dominated by in situ oxidation or experienced only minor supergene development (Fig. 12A).

Enriched porphyry Cu deposits (Fig. 12B): Porphyry Cu deposits with significant enrichment zones occur in the central and southern segments of the study area (Fig. 12A) and tend to have developed in orebodies where pyrite-rich alteration zones are preserved. Some host significant oxidized zones above the secondary sulfides that developed when acidity was insufficient to mobilize all the Cu from the hypogene ore (e.g., Toki cluster, Rivera et al., 2009) or from early formed enrichment zones (e.g., Chuquicamata, Ossandón et al., 2001; Polo Sur, Perelló et al., 2010). Enrichment appears to have been particularly efficient in telescoped deposits, where a high-sulfidation assemblage overprinted the potassic zone, introducing abundant acidity-generating pyrite and altering host rocks to phyllic or advanced argillic assemblages with low acid-buffering capacity. Examples include Chuquicamata, Escondida, and Escondida Norte-Zaldivar, which all have enrichment factors ≥3 (Sillitoe, 2005). Enrichment is also well developed in less telescoped porphyry Cu deposits with phyllic zones overlying potassic zones, such as Quebrada Blanca and Ujina, which have enrichment factors of ~2.4 (Sillitoe, 2005). Preservation of the relatively shallow phyllic and advanced argillic alteration zones probably requires fairly low postmineralization exhumation rates. In the Collahuasi district, this is supported by fluid inclusion pressure estimates from the Rosario porphyry Cu deposit, suggesting firstly that relatively fast synmineralization exhumation removed ~1 km of overburden between early potassic (~34.4 Ma) and late high-sulfidation (~32.6 Ma) epithermal assemblages, and secondly that <500 m of surface denudation occurred thereafter (Masterman et al., 2005). Slow postmineralization exhumation resulted in prolonged preservation of the upper parts of the hypogene orebodies, which enabled the formation of well-developed enrichment zones and may explain the apparent absence of outcropping plutonic rocks with ages <40 Ma in the vicinity of the porphyry Cu deposits. The preservation of shallowly emplaced, clinopyroxene-rich plutons in the Centinela and Escondida areas also supports slow postmineralization exhumation.

In situ oxidized porphyry Cu deposits (Fig. 12C): Some deposits within the study area lack major secondary sulfide zones but have been affected by significant in situ oxidation, such as at El Abra, Radomiro Tomic, Esperanza, and Telegrafo. These deposits are pyrite poor, and many are dominated by potassic alteration (Ambrus, 1977; Cuadra and Camus, 1998; Perelló et al., 2004, 2010; Sillitoe, 2005), which may indicate that pyrite-rich phyllic and advanced argillic zones once present above the potassic zone have been eroded, exposing relatively deep levels (Ambrus, 1977; Sillitoe, 2005). The 36.8 ± 0.2 Ma, 5.20 ± 1.10-km-deep sample SID-16-20 from the Pajonal-El Abra pluton supports deep erosion of the El Abra deposit. The pluton overlaps in age with the ~38–36 Ma El Abra porphyries (Ballard, 2001; Campbell et al., 2006; Correa et al., 2016), indicating ≥4 km of postmineralization exhumation. This is substantial, given that most porphyry Cu deposits are thought to form in the upper 5 km of the crust (Seedorff et al., 2005; Wilkinson and Kesler, 2007; Singer et al., 2008; Yanites and Kesler, 2015). Esperanza and Telegrafo are characterized by concentric alteration zoning patterns where pyrite-poor potassic cores (hosting the bulk of the Cu) presently reach near-surface levels and grade laterally to more pyrite-rich sericite-chlorite and phyllic alteration (Perelló et al., 2010). Erosion of potentially pyrite rich zones once present above the potassic cores may have prevented significant enrichment. Fluid inclusion data from Esperanza suggests that quartz veins formed 1–2 km below the water table (Perelló et al., 2004), which suggests a shallower erosional level but also a shallower emplacement depth compared to El Abra. Shallow emplacement is consistent with the high Au content at Esperanza and Telegrafo (Perelló et al., 2010) compared to the primarily Cu-Mo deposits that dominate the rest of the belt, since Cu-Au deposits are typically emplaced at shallower levels than Cu-Mo deposits (Cox and Singer, 1992; Sillitoe, 2000). Shallow emplacement is also supported by the abundant fine-grained intrusions in

the Centinela district, which lack hornblende in equilibrium. The Radomiro Tomic deposit is deeply oxidized but poorly enriched and also exposed at a level dominated by potassic alteration with only minor structurally controlled zones of phyllic alteration (Cuadra and Camus, 1998).

Porphyry Cu deposits with minor supergene development (Fig. 12D): The metallogenic belt also includes porphyry Cu deposits affected by only minor supergene modification. The Queen Elizabeth area in the northern segment (Fig. 12A) hosts relatively small, low-grade porphyry Cu deposits (Camus, 2003) that have experienced only minor supergene development. This is probably due to the presence of late Oligocene-early Miocene volcanic cover units that currently surround, and may once have covered, the Yabricoya and Alantaya plutons. The ~38 Ma (this study) Queen Elizabeth porphyry Cu deposit was already covered by volcanic rocks in the late Oligocene, before major supergene enrichment in other parts of the belt, and this likely inhibited supergene development. Erosion continued in the area after cover rocks were deposited (Morandé et al., 2015), resulting in partial reexposure of the deposit, but this may have happened outside or too close to the end of the supergene window. The ~40 Ma La Planada deposit (Gardeweg and Sellés, 2013; Tomlinson et al., 2015) is older than Queen Elizabeth and has been interpreted as a deeply eroded system (Eggers and Fuentes, 2019), which may partly explain the poor supergene development. However, the deposit may also once have been concealed beneath late Oligocene-early Miocene cover. Ministro Hales, on the western side of the West fault in the Chuquicamata district, has a poorly developed supergene profile compared to Chuquicamata and Radomiro Tomic on the eastern side (Sillitoe, 2005). Ministro Hales was exhumed to near-surface levels by 20.8 ± 0.6 Ma, as indicated by a supergene alunite K-Ar age (Sillitoe and McKee, 1996), but then covered by >50 m of alluvial gravels, indicating that it became located in a depositional environment that probably did not experience the required water table drop (Sillitoe et al., 1998). At the same time, Chuquicamata and Radomiro Tomic on the eastern side of the fault likely experienced relative water table drop and deep weathering (Sillitoe and McKee, 1996; Sillitoe et al., 1998; Sillitoe, 2005).

Porphyry Cu deposit potential in northernmost Chile: Age and emplacement depth data from plutons in the Inti area suggest that Eocene plutons representing a crustal paleodepth similar to that of areas farther south in the metallogenic belt were exposed at the surface prior to late Oligocene-early Miocene volcanism. Thus, potential middle Eocene-early Oligocene porphyry Cu deposits could also have reached the surface prior to deposition. The ~35 Ma plutons (samples C86 and C88) suggest that an even greater thickness of rock has been exhumed at a later stage at Inti than in other parts of the belt in order to have exposed such young plutons. However, these plutons lack emplacement depth constraints due to an absence of hornblende and could have been emplaced at shallow levels (<4 km). Despite exhumation histories similar to those of economically richer parts of the belt, the volcaniclastic units, which likely terminated supergene processes, were deposited already in the early Miocene. The only possible window for supergene enrichment of potential porphyry Cu deposits is therefore prior to deposition of the cover. The requisite time is not known, but, based on the span of supergene alunite ages from Escondida and Chuquicamata, supergene enrichment processes lasted for at least ~3 to ~5 m.y. (Alpers and Brimhall, 1988; Sillitoe and McKee, 1996). Taking 3 m.y. as a minimum time to develop a mature supergene blanket in an arid environment would require porphyry Cu deposits at Inti to have been exposed at or near the surface by ~25 Ma and located in a favorable environment for supergene enrichment until cover deposition at ~22 Ma. Sample C91 suggests that the Eocene magmatic arc in the Inti area underwent exhumation at an average rate of 0.326 ± 0.032 km/m.y. between ~40 and ~22 Ma, which is probably too high to enable appreciable supergene enrichment in an arid environment. A situation where the rate of exhumation was higher toward the start of the time interval and significantly lower just prior to the time of burial beneath volcanic cover is possible and could have created favorable supergene conditions toward the late Oligocene. However, the reconstructed late Oligocene paleolandscape suggests that the Precordillera in this area was cut by ~500-m-deep EW-directed paleochannels that transported conglomerates of the Azapa Formation into the Central depression (van Zalinge et al., 2017). Such a landscape is different from a pediplain of the type known to be favorable for supergene enrichment (Bouzari and Clark, 2002; Riquelme et al., 2017; Sanchez et al., 2018), suggesting that the Precordillera in northernmost Chile was a highly erosive terrane until the volcanic cover was deposited. Inti therefore appears to be an area where extensive postexhumation cover was detrimental to supergene development.

Conclusions

Despite having Carboniferous-Eocene emplacement ages spanning almost 300 m.y., most plutonic rocks in the middle Eocene-early Oligocene metallogenic belt in the Precordillera of northern Chile (17.8°–24.2°S) have remarkably similar emplacement depths of ~4 to ~7 km. This is inconsistent with a unidirectional exhumation model and likely reflects a more complex history of exhumation and burial.

Two periods of net exhumation can be defined: (1) early Permian-Middle Triassic, when Carboniferous-Permian plutons were exhumed and exposed at the surface and (2) middle Eocene-late Oligocene, when Eocene plutons were exhumed and exposed. Preservation of both Carboniferous-Permian and Eocene plutons at the surface today requires a period of net burial between the Late Triassic and middle Eocene, during which a dominantly extensional regime prevailed in northern Chile. Preservation of plutons today that were exposed by the late Oligocene-early Miocene also requires low exhumation rates since this time.

Hypogene mineralization in the middle Eocene-early Oligocene porphyry Cu deposits occurred at a time of relatively fast exhumation (>0.10 km/m.y.), consistent with previous thermochronology studies and with models suggesting that high exhumation rates favor hypogene ore formation by promoting efficient fluid exsolution and facilitating telescoping. Supergene mineralization, on the other hand, occurred when average exhumation rates were lower (<~0.01 km/m.y.). Slow exhumation would have created a favorable balance between surface denudation and relative water table descent, allowing enough time for Cu to be leached and transported down to

the paleowater table before it was lost to surface erosion. This likely enabled the formation and preservation of supergene enrichment zones.

Even though the regional exhumation history of the middle Eocene-early Oligocene belt was favorable for both hypogene and supergene mineralization, supergene enrichment appears to have been hampered where the exhumed crustal thickness following hypogene mineralization was substantial (e.g., ≥~4 km at El Abra) or where porphyry Cu deposits were buried beneath significant cover (e.g., Queen Elizabeth, Ministro Hales). In the Inti region, extensive late Oligocene-early Miocene volcanic cover would have terminated nascent supergene enrichment processes within any near-surface porphyry Cu deposits, while exhumation rates prior to cover deposition were probably too high to enable effective supergene enrichment to initiate.

Acknowledgments

This work was funded by BHP. We are grateful to all the BHP staff in Chile who helped us with field work, particularly Carlos Galdames, Aldo Vásquez, Jamie King, Chris Ford, Guilherme Andrade Santos, and Walter Jimenez. All sampling was conducted with written permission from mining and exploration companies holding exploration permits. We thank Anglo American, Antofagasta Minerals, Codelco, Collahuasi, ENAMI, Freeport-McMoran, Glencore, Minera Escondida, Minera Meridian, Sumitomo Corporation, Teck Resources, and Vale for granting us sampling permission. We thank Edward Bunker, Luke Neal, and Anne Mather for field assistance; Dan Condon at the British Geological Survey for field assistance and helpful discussions about U-Pb geochronology; Stuart Kearns and Ben Buse for technical assistance with the SEM and electron microprobe; Vanessa Pashley and Matthew Horstwood at the British Geological Survey for help with the U-Pb analyses; Tom Knott and Lin Marvin-Dorland at the University of Leicester for help with whole-rock geochemistry analyses; and Isa Witick for assistance with compiling the final manuscript. We appreciate the constructive reviews provided by Jose Piquer, Eduardo Campos, and David Cooke, and we thank Larry Meinert and David Cooke for their editorial handling of the manuscript.

REFERENCES

Adams, B.A., Hodges, K.V., Whipple, K.X., Ehlers, T.A., Van Soest, M.C., and Wartho, J., 2015, Constraints on the tectonic and landscape evolution of the Bhutan Himalaya from thermochronometry: Tectonics, v. 34, p. 1329–1347.

Alpers, C.N., and Brimhall, G.H., 1988, Middle Miocene climatic change in the Atacama Desert, northern Chile: Evidence from supergene mineralization at La Escondida: Bulletin of the Geological Society of America, v. 100, p. 1640–1656.

Ambrus, J., 1977, Geology of the El Abra porphyry copper deposit, Chile: Economic Geology, v. 72, p. 1062–1085.

Amilibia, A., Sàbat, F., McClay, K.R., Muñoz, J.A., Roca, E., and Chong, G., 2008, The role of inherited tectono-sedimentary architecture in the development of the central Andean mountain belt: Insights from the Cordillera de Domeyko: Journal of Structural Geology, v. 30, p. 1520–1539.

Anderson, J.L., and Smith, D.R., 1995, The effects of temperature and f_{O_2} on the Al-in-hornblende barometer: American Mineralogist, v. 80, p. 549–559.

Annen, C., Blundy, J.D., and Sparks, R.S.J., 2006, The genesis of intermediate and silicic magmas in deep crustal hot zones: Journal of Petrology, v. 47, p. 505–539.

Arancibia, G., Matthews, S.J., and Pérez de Arce, C., 2006, K-Ar and $^{40}Ar/^{39}Ar$ geochronology of supergene processes in the Atacama Desert, northern Chile: Tectonic and climatic relations: Journal of the Geological Society, London, v. 163, p. 107–118.

Ardill, J., Flint, S., Chong, G., and Wilke, H., 1998, Sequence stratigraphy of the Mesozoic Domeyko basin, northern Chile: Journal of the Geological Society, London, v. 155, p. 71–88.

Armijo, R., Lacassin, R., Coudurier-Curveur, A., and Carrizo, D., 2015, Coupled tectonic evolution of Andean orogeny and global climate: Earth-Science Reviews, v. 143, p. 1–35.

Arriagada, C., 2018, Tectonic rotations along the western central Andes, *in* Folguera, A., Contreras Reyes, E., Heredia, N., Encinas, A., Iannelli, S.B., et al., eds., The evolution of the Chilean-Argentinean Andes: Cham, Switzerland, Springer, p. 329–341.

Avdievitch, N.N., Ehlers, T.A., and Glotzbach, C., 2018, Slow long-term exhumation of the west central Andean plate boundary, Chile: Tectonics, v. 37, p. 2243–2267.

Baker, M.C.W., and Francis, P.W., 1978, Upper Cenozoic volcanism in the Central Andes—ages and volumes: Earth and Planetary Science Letters, v. 41, p. 175–187.

Ballard, J., 2001, A comparative study between the geochemistry of ore-bearing and barren calc-alkaline intrusions: Unpublished Ph.D. thesis, Canberra, Australia, Australian National University, 255 p.

Barnes, J.B., and Ehlers, T.A., 2009, End member models for Andean Plateau uplift: Earth-Science Reviews, v. 97, p. 105–132.

Bissig, T., and Riquelme, R., 2009, Contrasting landscape evolution and development of supergene enrichment in the El Salvador porphyry Cu and Potrerillos-El Hueso Cu-Au districts, northern Chile: Society of Economic Geologists, Special Publication 14, p. 59–68.

——2010, Andean uplift and climate evolution in the southern Atacama Desert deduced from geomorphology and supergene alunite-group minerals: Earth and Planetary Science Letters, v. 299, p. 447–457.

Bisso, C.B., Duran, M., and Gonzales, A.A., 1998, Geology of the Ujina and Rosario porphyry copper deposits, Collahuasi district, Chile, *in* Porter, T.M. ed., Porphyry and hydrothermal copper and gold deposits: A global perspective: Adelaide, PGC Publishing, p. 133–148.

Blundy, J.D., and Holland, T.J.B., 1990, Calcic amphibole equilibria and a new amphibole-plagioclase geothermometer: Contributions to Mineralogy and Petrology, v. 104, p. 208–224.

Boric, R., Diaz, J., Becerra, H., and Zentilli, M., 2009, Geology of the Ministro Hales mine (MMH), Chuquicamata district, Chile [ext. abs.]: Congreso Geológico Chileno, 12th, Santiago, Chile, 2009, Extended Abstracts, p. 1–4.

Bouzari, F., and Clark, A.H., 2002, Anatomy, evolution, and metallogenic significance of the supergene orebody of the Cerro Colorado porphyry copper deposit, I region, northern Chile: Economic Geology, v. 97, p. 1701–1740.

Brimhall, G.H., Alpers, C.N., and Cunningham, A.R., 1985, Analysis of supergene ore-forming processes and ground-water solute transport using mass balance principles: Economic Geology, v. 80, p. 1227–1256.

Bunker, E., 2020, The hypogene evolution of the Spence porphyry copper deposit, northern Chile: Unpublished Ph.D. thesis, Bristol, United Kingdom, University of Bristol, 240 p.

Campbell, I.H., Ballard, J.R., Palin, J.M., Allen, C., and Faunes, A., 2006, U-Pb zircon geochronology of granitic rocks from the Chuquicamata-El Abra porphyry copper belt of northern Chile: Excimer laser ablation ICP-MS analysis: Economic Geology, v. 101, p. 1327–1344.

Camus, F., 2003, Geología de los sistemas porfídicos en los Andes de Chile: Santiago, Chile, Servicio Nacional de Geología y Minería (SERNAGEOMIN), 267 p.

Candela, P.A., 1997, A review of shallow, ore-related granites: Textures, volatiles, and ore metals: Journal of Petrology, v. 38, p. 1619–1633.

Carretier, S., Tolorza, V., Regard, V., Aguilar, G., Bermúdez, M.A., Martinod, J., Guyot, J.L., Hérail, G., and Riquelme, R., 2018, Review of erosion dynamics along the major N-S climatic gradient in Chile and perspectives: Geomorphology, v. 300, p. 45–68.

Chappell, B.W., White, A.J.R., Williams, I.S., and Wyborn, D., 2004, Low- and high-temperature granites: Earth and Environmental Science Transactions of the Royal Society of Edinburgh, v. 95, p. 125–140.

Charrier, R., Pinto, L., and Rodríguez, M.P., 2007, Tectonostratigraphic evolution of the Andean orogen in Chile, *in* Moreno, T., and Gibbons, W., eds., The geology of Chile: London, The Geological Society of London, p. 21–114.

Charrier, R., Hérail, G., Pinto, L., García, M., Riquelme, R., Farías, M., and Muñoz, N., 2013, Cenozoic tectonic evolution in the Central Andes in northern Chile and west central Bolivia: Implications for paleogeographic,

magmatic and mountain building evolution: International Journal of Earth Sciences, v. 102, p. 235–264.
Chaussard, E., and Amelung, F., 2014, Regional controls on magma ascent and storage in volcanic arcs: Geochemistry, Geophysics, Geosystems, v. 15, p. 1407–1418.
Chávez, W.X.J., 2000, Supergene oxidation of copper deposits: Zoning and distribution of copper oxide minerals: Society of Economic Geologists, SEG Newsletter, no. 41, p. 1, 10–21.
Chivas, A.R., O'Neil, J.R., and Katchan, G., 1984, Uplift and submarine formation of some Melanesian porphyry copper deposits: Stable isotope evidence: Earth and Planetary Science Letters, v. 68, p. 326–334.
Clark, A.H., Farrar, E., Kontak, D.J., Langridge, R.L., Arenas, M.J., France, L.J., McBride, S.L., Woodman, P.L., Wasteneys, H.A., Sandeman, H.A., and Archibald, D.A., 1990, Geologic and geochronologic constraints on the metallogenic evolution of the Andes of southeastern Peru: Economic Geology, v. 85, p. 1520–1583.
Clarke, J.D.A., 2006, Antiquity of aridity in the Chilean Atacama Desert: Geomorphology, v. 73, p. 101–114.
Coira, B., Davidson, J., Mpodozis, C., and Ramos, V., 1982, Tectonic and magmatic evolution of the Andes of northern Argentina and Chile: Earth Science Reviews, v. 18, p. 303–332.
Cooke, D.R., Hollings, P., and Walshe, J.L., 2005, Giant porphyry deposits: Characteristics, distribution, and tectonic controls: Economic Geology, v. 100, p. 801–818.
Cooper, F.J., Adams, B.A., Blundy, J.D., Farley, K.A., McKeon, R.E., and Ruggiero, A., 2016, Aridity-induced Miocene canyon incision in the Central Andes: Geology, v. 44, p. 675–678.
Cornejo, P., Tosdal, R.M., Mpodozis, C., Tomlinson, A.J., Rivera, O., and Fanning, C.M., 1997, El Salvador, Chile porphyry copper deposit revisited: Geologic and geochronologic framework: International Geology Review, v. 39, p. 22–54.
Cornejo, P., Matthews, S., and Pérez de Arce, C., 2003, The "K-T" compressive deformation event in northern Chile (24°–27° S) [ext. abs.]: Congreso Geológico Chileno, 10th, Concepción, Chile, 2003, Extended Abstracts, p. 1–13.
Cornejo, P., Tomlinson, A.J., Mora, R., and Ojeda, G., 2019, Preservation of subeconomic Permian-Triassic porphyry Cu and epithermal deposits in Central Andes contradict exhumation models for temporal distribution of ore deposits [ext. abs.]: Society of Economic Geologists, SEG 2019: South American Metallogeny: Sierra to Craton, Santiago, Chile, October 7–10, 2019, Proceedings.
Correa, K.J., Rabbia, O.M., Hernández, L.B., Selby, D., and Astengo, M., 2016, The timing of magmatism and ore formation in the El Abra porphyry copper deposit, northern Chile: Implications for long-lived multiple-event magmatic-hydrothermal porphyry systems: Economic Geology, v. 111, p. 1–28.
Cox, D.P., and Singer, D.A., 1992, Gold—distribution of gold in porphyry copper deposits: U.S. Geological Survey, Bulletin 1877, p. C1-C14.
Cuadra, P., and Camus, F., 1998, The Radomiro Tomic porphyry copper deposit, northern Chile, *in* Porter, T.M., ed., Porphyry and hydrothermal copper and gold deposits: A global perspective: Adelaide, PGC Publishing, p. 99–110.
Damm, K.W., Pichowiak, S., Harmon, R.S., Todt, W., Kelley, S., Omarini, R., and Niemeyer, H., 1990, Pre-Mesozoic evolution of the central Andes; the basement revisited: Geological Society of America, Special Paper 241, p. 101–126.
del Rey, A., Deckart, K., Arriagada, C., and Martínez, F., 2016, Resolving the paradigm of the late Paleozoic-Triassic Chilean magmatism: Isotopic approach: Gondwana Research, v. 37, p. 172–181.
Dick, L.A., Ossandón C.G., Fitch, R.G., Swift Jr., C.M., and Watts, A., 1993, Discovery of blind copper mineralization at Collahuasi, Chile [ext. abs.]: Society of Economic Geologists, SEG 1993 Conference, Denver, Colorado, USA, 1993, Conference Program and Extended Abstracts, p. AB21–AB23.
Dunai, T.J., González López, G.A., and Juez-Larré, J., 2005, Oligocene-Miocene age of aridity in the Atacama Desert revealed by exposure dating of erosion-sensitive landforms: Geology, v. 33, p. 321–324.
Eggers, T., and Fuentes, G., 2019, New structural insights from the Yabricoya porphyry: "Reverse graben" architecture masked within an uplifted tectonic pillar and their district exploration consequences [ext. abs.]: Society of Economic Geologists, SEG 2019: South American Metallogeny: Sierra to Craton: Santiago, Chile, October 7–10, 2019, Proceedings.
Emmons, W.H., 1917, The enrichment of ore deposits: U.S. Geological Survey, Bulletin 625, 530 p.
Enders, M.S., Knickerbocker, C., Titley, S.R., and Southam, G., 2006, The role of bacteria in the supergene environment of the Morenci porphyry copper deposit, Greenlee County, Arizona: Economic Geology, v. 101, p. 59–70.
Evenstar, L.A., Hartley, A.J., Stuart, F.M., Mather, A.E., Rice, C.M., and Chong, G., 2009, Multiphase development of the Atacama planation surface recorded by cosmogenic ^{3}He exposure ages: Implications for uplift and Cenozoic climate change in Western South America: Geology, v. 37, p. 27–30.
Evenstar, L.A., Mather, A.E., Hartley, A.J., Stuart, F.M., Sparks, R.S.J., and Cooper, F.J., 2017, Geomorphology on geologic timescales: Evolution of the late Cenozoic Pacific paleosurface in northern Chile and southern Peru: Earth-Science Reviews, v. 171, p. 1–27.
Farías, M., Charrier, R., Comte, D., Martinod, J., and Hérail, G., 2005, Late Cenozoic deformation and uplift of the western flank of the Altiplano: Evidence from the depositional, tectonic, and geomorphologic evolution and shallow seismic activity (northern Chile at 19°30'S): Tectonics, v. 24, p. 1–27.
Farley, K.A., 2000, Helium diffusion from apatite: General behavior as illustrated by Durango fluorapatite: Journal of Geophysical Research: Solid Earth, v. 105, p. 2903–2914.
Freymuth, H., Brandmeier, M., and Wörner, G., 2015, The origin and crust/mantle mass balance of Central Andean ignimbrite magmatism constrained by oxygen and strontium isotopes and erupted volumes: Contributions to Mineralogy and Petrology, v. 169, p. 1–24.
Galli-Olivier, C., 1967, Pediplain in northern Chile and the Andean uplift: Science, v. 158, p. 653–655.
García, M., Gardeweg, M., Clavero, J., and Hérail, G., 2004, Hoja Arica: Region de Tarapacá: Servicio Nacional de Geología y Minería, Carta Geológica de Chile, Serie Geología Básica, no. 84, 1 map, scale 1:250,000.
García, M., Maksaev, V., Townley, B., and Dilles, J., 2017, Metallogeny, structural evolution, post-mineral cover distribution and exploration in concealed areas of the northern Chilean Andes: Ore Geology Reviews, v. 86, p. 652–672.
Gardeweg, M., and Sellés, D., 2013, Geología del área Collacagua-Rinconada, región de Tarapacá: Servicio Nacional de Geología y Minería, Carta Geológica de Chile, Serie Geología Básica, no. 148, 1 map, scale 1:100,000.
Götze, H.-J., and Kirchner, A., 1997, Interpretation of gravity and geoid in the Central Andes between 20° and 29°S: Journal of South American Earth Sciences, v. 10, p. 179–188.
Gröschke, M., and Wilke, H.-G., 1986, Lithology and stratigraphy of Jurassic sediments in the north Chilean pre-cordillera between 21°30′ and 22°S: Zentralblatt für Geologie und Paläontologie, Teil I, v. 1985, p. 1317–1324.
Hammarstrom, J.M., and Zen, E., 1986, Aluminum in hornblende: An empirical igneous geobarometer: American Mineralogist, v. 71, p. 1297–1313.
Hartley, A.J., and Rice, C.M., 2005, Controls on supergene enrichment of porphyry copper deposits in the Central Andes: A review and discussion: Mineralium Deposita, v. 40, p. 515–525.
Hartley, A.J., Chong, G., Houston, J., and Mather, A.E., 2005, 150 million years of climatic stability: Evidence from the Atacama Desert, northern Chile: Journal of the Geological Society, London, v. 162, p. 421–424.
Haschke, M., Siebel, W., Günther, A., and Scheuber, E., 2002, Repeated crustal thickening and recycling during the Andean orogeny in north Chile (21°–26°S): Journal of Geophysical Research: Solid Earth, v. 107, p. ECV 6-1-ECV 6-18.
Hervé, M., Sillitoe, R.H., Wong, C., Fernández, P., Crignola, F., Ipinza, M., and Urzúa, F., 2012, Geologic overview of the Escondida porphyry copper district, northern Chile: Society of Economic Geologists, Special Publication 16, p. 55–78.
Holland, T., and Blundy, J., 1994, Non-ideal interactions in calcic amphiboles and their bearing on amphibole-plagioclase thermometry: Contributions to Mineralogy and Petrology, v. 116, p. 433–447.
Hollister, L.S., Grissom, G.C., Peters, E.K., Stowell, H.H., and Sisson, V.B., 1987, Confirmation of the empirical correlation of Al in hornblende with pressure of solidification of calc-alkaline plutons: American Mineralogist, v. 72, p. 231–239.
Holtz, F., and Johannes, W., 1994, Maximum and minimum water contents of granitic melts: Implications for chemical and physical properties of ascending magmas: Lithos, v. 32, p. 149–159.
Horstwood, M.S.A., Košler, J., Gehrels, G., Jackson, S.E., McLean, N.M., Paton, C., Pearson, N.J., Sircombe, K., Sylvester, P., Vermeesch, P., Bowring, J.F., Condon, D.J., and Schoene, B., 2016, Community-derived standards for LA-ICP-MS U-(Th-)Pb geochronology: Uncertainty propagation,

age interpretation and data reporting: Geostandards and Geoanalytical Research, v. 40, p. 311–332.
Ireland, T., 2010, Geological framework of the mineral deposits of the Collahuasi district, Región de Tarapacá, Chile: Unpublished Ph.D. thesis, Hobart, Australia, University of Tasmania, Centre for Ore Deposit and Earth Sciences (CODES), 466 p.
Johnson, M.C., and Rutherford, M.J., 1989, Experimental calibration of the aluminium-in-hornblende geobarometer with application to Long Valley caldera: Geology, v. 17, p. 837–841.
Jordan, T.E., Kirk-Lawlor, N.E., Nicolás Blanco, P., Rech, J.A., and Cosentino, N.J., 2014, Landscape modification in response to repeated onset of hyperarid paleoclimate states since 14 Ma, Atacama Desert, Chile: Bulletin of the Geological Society of America, v. 126, p. 1016–1046.
Juez-Larré, J., Kukowski, N., Dunai, T.J., Hartley, A.J., and Andriessen, P.A.M., 2010, Thermal and exhumation history of the Coastal Cordillera arc of northern Chile revealed by thermochronological dating: Tectonophysics, v. 495, p. 48–66.
Kay, S.M., Mpodozis, C., and Coira, B., 1999, Neogene magmatism, tectonism and mineral deposits of the Central Andes (22°–23°S latitude): Society of Economic Geologists, Special Publication 7, p. 27–59.
Kober, F., Ivy-Ochs, S., Schlunegger, F., Baur, H., Kubik, P.W., and Wieler, R., 2007, Denudation rates and a topography-driven rainfall threshold in northern Chile: Multiple cosmogenic nuclide data and sediment yield budgets: Geomorphology, v. 83, p. 97–120.
Kukowski, N., and Oncken, O., 2006, Subduction erosion—the "normal" mode of fore-arc material transfer along the Chilean margin?, *in* Oncken, O., Chong, G., Franz, G., Giese, P., Götze, H.-J., Ramos, V., Strecker, M., and Wigger, P., eds., The Andes: Berlin/Heidelberg, Springer Verlag, p. 217–236.
Kurtz, A.C., Kay, S.M., Charrier, R., and Farrar, E., 1997, Geochronology of Miocene plutons and exhumation history of the El Teniente region, Central Chile (34–35 degrees S): Revista Geologica de Chile, v. 24, p. 75–90.
Leake, B.E., Woolley, A.R., Arps, C.E.S., Birch, W.D., Gilbert, M.C., Grice, J.D., Hawthorne, F.C., Kato, A., Kisch, H.J., Krivovichev, V.G., et al., 1997, Nomenclature of amphiboles; report of the subcommittee on amphiboles of the International Mineralogical Association Commission on New Minerals and Mineral Names: Mineralogical Magazine, v. 61, p. 295–310.
Lindsay, D.D., Zentilli, M., and Rivera, J.R.D.L., 1995, Evolution of an active ductile to brittle shear system controlling mineralization at the Chuquicamata porphyry copper deposit, northern Chile: International Geology Review, v. 37, p. 945–958.
Llambías, E.J., and Sato, A.M., 1990, El batolito de Colangüil (29–31°S) Cordillera Frontal de Argentina: Estructura y marco tectónico: Revista Geológica de Chile, v. 17, p. 89–108.
Loewy, S.L., Connelly, J.N., and Dalziel, I.W.D., 2004, An orphaned basement block: The Arequipa-Antofalla basement of the central Andean margin of South America: Bulletin of the Geological Society of America, v. 116, p. 171–187.
Lucassen, F., Franz, G., and Laber, A., 1999, Permian high pressure rocks—the basement of the Sierra de Limon Verde in northern Chile: Journal of South American Earth Sciences, v. 12, p. 183–199.
Lucassen, F., Becchio, R., Harmon, R., Kasemann, S., Franz, G., Trumbull, R., Wilke, H.G., Romer, R.L., and Dulski, P., 2001, Composition and density model of the continental crust at an active continental margin: The Central Andes between 21° and 27°S: Tectonophysics, v. 341, p. 195–223.
Ludwig, K.R., 2012, User's manual for Isoplot version 3.75–4.15: A geochronological toolkit for Microsoft Excel: Berkley Geochronological Center, Special Publication 5, 75 p.
Maksaev, V., 1990, Metallogeny, geological evolution and thermochronology of the Chilean Andes between latitudes 21° and 26° south, and the origin of major porphyry copper deposits: Unpublished Ph.D. thesis, Halifax, Canada, Dalhousie University, 544 p.
Maksaev, V., and Zentilli, M., 1999, Fission track thermochronology of the Domeyko Cordillera, northern Chile; implications for Andean tectonics and porphyry copper metallogenesis: Exploration and Mining Geology, v. 8, p. 65–89.
Maksaev, V., Townley, B., Palacios, C., and Camus, F., 2007, Metallic ore deposits, *in* Moreno, T., and Gibbons, W., eds., The geology of Chile: London, The Geological Society of London, p. 179–199.
Maksaev, V., Munizaga, F., and Tassinari, C., 2014, Timing of the magmatism of the paleo-Pacific border of Gondwana: U-Pb geochronology of late Paleozoic to early Mesozoic igneous rocks of the north Chilean Andes between 20° and 31°S: Andean Geology, v. 41, p. 447–506.
Marquardt, J.C., Pizarro, L.J., Gomez del V.A., and Martinez, A., 1997, Prospecto Lila, descubrimiento de un pórfido cuprífero Triásico Superior-Jurásico Inferior en la Cordillera de Domeyko, II Región, Chile [ext. abs.]: Congreso Geológico Chileno, 8th, Antofagasta, Chile, 1997, Proceedings, v. 2, p. 1048–1053.
Marsh, T.M., Einaudi, M.T., and McWilliams, M., 1997, $^{40}Ar/^{39}Ar$ geochronology of Cu-Au and Au-Ag mineralization in the Potrerillos district, Chile: Economic Geology, v. 92, p. 784–806.
Masterman, G.J., 2003, Structural and geochemical evolution of the Rosario copper-molybdenum porphyry deposit and related copper-silver veins, Collahuasi district: Unpublished Ph.D. thesis, Tasmania, Australia, University of Tasmania, 253 p.
Masterman, G.J., Cooke, D.R., Berry, R.F., Clark, A.H., Archibald, D.A., Mathur, R., Walshe, J.L., and Durán, M., 2004, $^{40}Ar/^{39}Ar$ and Re-Os geochronology of porphyry copper-molybdenum deposits and related copper-silver veins in the Collahuasi district, northern Chile: Economic Geology, v. 99, p. 673–690.
Masterman, G. J., Cooke, D.R., Berry, R.F., Walshe, J.L., Lee, A.W., and Clark, A.H., 2005, Fluid chemistry, structural setting, and emplacement history of the Rosario Cu-Mo porphyry and Cu-Ag-Au epithermal veins, Collahuasi district, northern Chile: Economic Geology, v. 100, p. 835–862.
Maydagán, L., Franchini, M., Rusk, B., Lentz, D.R., McFarlane, C., Impiccini, A., Ríos, F.J., and Rey, R., 2015, Porphyry to epithermal transition in the Altar Cu-(Au-Mo) deposit, Argentina, studied by cathodoluminescence, LA-ICP-MS, and fluid inclusion analysis: Economic Geology, v. 110, p. 889–923.
McInnes, B.I.A., Farley, K.A., Sillitoe, R.H., and Kohn, B.P., 1999, Application of apatite (U-Th)/He thermochronometry to the determination of the sense and amount of vertical fault displacement at the Chuquicamata porphyry copper deposit, Chile: Economic Geology, v. 94, p. 937–947.
Mégard, F., 1987, Cordilleran Andes and marginal Andes: A review of Andean geology north of the Arica elbow (18°S), *in* Monger, J., and Francheteau, J., eds., Circum-Pacific orogenic belts and evolution of the Pacific Ocean basin: American Geophysical Union, Geodynamic Series, v. 18, p. 71–95.
Morandé, J., Gallardo, F., Muñoz, M., and Farías, M., 2015, Carta Guaviña, Región de Tarapacá: Servicio Nacional de Geología y Minería, Carta Geológica de Chile, Serie Geología Básica, no. 177, 1 map, scale 1:100,000.
Mortimer, C., 1973, The Cenozoic history of the southern Atacama Desert, Chile: Journal of the Geological Society, London, v. 129, p. 505–526.
Mote, T.I., Brimhall, G.H., Tidy-Finch, E., Muller, G., and Carrasco, P., 2001, Application of mass-balance modeling of sources, pathways, and sinks of supergene enrichment to exploration and discovery of the Quebrada Turquesa exotic copper orebody, El Salvador district, Chile: Economic Geology, v. 96, p. 367–386.
Mpodozis, C., and Cornejo, P., 2012, Cenozoic tectonics and porphyry copper systems of the Chilean Andes: Society of Economic Geologists, Special Publication 16, p. 329–360.
Mpodozis, C., Arriagada, C., Basso, M., Roperch, P., Cobbold, P., and Reich, M., 2005, Late Mesozoic to Paleogene stratigraphy of the Salar de Atacama basin, Antofagasta, northern Chile: Implications for the tectonic evolution of the Central Andes: Tectonophysics, v. 399, p. 125–154.
Munizaga, F., Maksaev, V., Fanning, C.M., Giglio, S., Yaxley, G., and Tassinari, C.C.G., 2008, Late Paleozoic-Early Triassic magmatism on the western margin of Gondwana: Collahuasi area, northern Chile: Gondwana Research, v. 13, p. 407–427.
Murray, K.E., Braun, J., and Reiners, P.W., 2018, Toward robust interpretation of low-temperature thermochronometers in magmatic terranes: Geochemistry, Geophysics, Geosystems, v. 19, p. 3739–3763.
Mutch, E.J.F., Blundy, J.D., Tattitch, B.C., Cooper, F.J., and Brooker, R.A., 2016, An experimental study of amphibole stability in low-pressure granitic magmas and a revised Al-in-hornblende geobarometer: Contributions to Mineralogy and Petrology, v. 171, p. 1–27.
Niemeyer, H., Götze, J., Sanhueza, M., and Portilla, C., 2018, The Ordovician magmatic arc in the northern Chile-Argentina Andes between 21° and 26° south latitude: Journal of South American Earth Sciences, v. 81, p. 204–214.
Oliveros, V., Vásquez, P., Creixell, C., Lucassen, F., Ducea, M.N., Ciocca, I., González, J., Espinoza, M., Salazar, E., Coloma, F., and Kasemann, S.A., 2020, Lithospheric evolution of the Pre- and Early Andean convergent margin, Chile: Gondwana Research, v. 80, p. 202–227.
Ossandón, G., Fréraut, R., Gustafson, L.B., Lindsay, D.D., and Zentilli, M., 2001, Geology of the Chuquicamata mine: A progress report: Economic Geology, v. 96, p. 249–270.

Padilla Garza, R.A., Titley, S.R., and Pimentel B., F., 2001, Geology of the Escondida porphyry copper deposit, Antofagasta region, Chile: Economic Geology, v. 96, p. 307–324.

Pamukcu, A.S., Gualda, G.A.R., Ghiorso, M.S., Miller, C.F., and McCracken, R.G., 2015, Phase-equilibrium geobarometers for silicic rocks based on rhyolite-MELTS—part 3: Application to the Peach Spring tuff (Arizona-California-Nevada, USA): Contributions to Mineralogy and Petrology, v. 169, p. 1–17, doi: 10.1007/s00410-015-1122-y.

Paton, C., Hellstrom, J., Paul, B., Woodhead, J., and Hergt, J., 2011, Iolite: Freeware for the visualisation and processing of mass spectrometric data: Journal of Analytical Atomic Spectrometry, v. 26, p. 2508–2518.

Perelló, J., 2003, Conchi porphyry copper deposit, Antofagasta region, northern Chile [ext. abs.]: Congreso Geológico Chileno, 10th, Concepción, Chile, 2003, Extended Abstracts.

Perelló, J., Brockway, H., and Martini, R., 2004, Discovery and geology of the Esperanza porphyry copper-gold deposit, Antofagasta region, northern Chile: Society of Economic Geologists, Special Publication 11, p. 167–186.

Perelló, J., Muhr, R., Mora, R., Martínez, E., Brockway, H., Artal, J., Mpodozis, C., Munchmeyer, C., Clifford, J., Acuña, E., Swaneck, T., Valenzuela, E., and Argandoña, R., 2010, Wealth creation through exploration in a mature terrain: The case history of the Centinela district, northern Chile porphyry copper belt: Society of Economic Geologists, Special Publication 15, p. 229–252.

Piwinskii, A.J., and Wyllie, P.J., 1970, Experimental studies of igneous rock series; felsic body suite from the Needle Point pluton, Wallowa batholith, Oregon: Journal of Geology, v. 78, p. 52–76.

Platzman, E.S., Sparks, R.S.J., and Cooper, F.J., 2020, Fabrics, facies, and flow through a large-volume ignimbrite: Pampa De Oxaya, Chile: Bulletin of Volcanology, v. 82, p. 1–19.

Prezzi, C.B., Götze, H.J., and Schmidt, S., 2009, 3D density model of the Central Andes: Physics of the Earth and Planetary Interiors, v. 177, p. 217–234.

Quang, C.X., Clark, A.H., Lee, J.K.W., and Guillen B., J., 2003, ^{40}Ar-^{39}Ar ages of hypogene and supergene mineralization in the Cerro Verde-Santa Rosa porphyry Cu-Mo cluster, Arequipa, Peru: Economic Geology, v. 98, p. 1683–1696.

Quang, C.X., Clark, A.H., Lee, J.K.W., and Hawkes, N., 2005, Response of supergene processes to episodic Cenozoic uplift, pediment erosion, and ignimbrite eruption in the porphyry copper province of southern Perú: Economic Geology, v. 100, p. 87–114.

Rabbia, O.M., Correa, K.J., Hernández, L.B., and Ulrich, T., 2017, "Normal" to adakite-like arc magmatism associated with the El Abra porphyry copper deposit, Central Andes, northern Chile: International Journal of Earth Sciences, v. 106, p. 2687–2711.

Ramos, V.A., and Folguera, A., 2009, Andean flat-slab subduction through time: Geological Society, London, Special Publication 327, p. 31–54.

Rapalini, A.E., 1989, Estudio paleomagnético del vulcanismo permotriásico de la región andina de la República Argentina: Consecuencias tectónicas y geodinámicas: Unpublished Ph.D. thesis, Buenos Aires, Argentina, Universidad de Buenos Aires, 278 p.

Rech, J.A., Currie, B.S., Jordan, T.E., Riquelme, R., Lehmann, S.B., Kirk-Lawlor, N.E., Li, S., and Gooley, J.T., 2019, Massive middle Miocene gypsic paleosols in the Atacama Desert and the formation of the Central Andean rain-shadow: Earth and Planetary Science Letters, v. 506, p. 184–194.

Reich, M., and Vasconcelos, P.M., 2015, Geological and economic significance of supergene metal deposits: Elements, v. 11, p. 305–310.

Reiners, P.W., Thomson, S.N., Vernon, A., Willett, S.D., Zattin, M., Einhorn, J., Gehrels, G., Quade, J., Pearson, D., Murray, K.E., and Cavazza, W., 2015, Low-temperature thermochronologic trends across the central Andes, 21°S-28°S: Geological Society of America, Memoir 212, p. 215–249.

Reutter, K.-J., Scheuber, E., and Helmcke, D., 1991, Structural evidence of orogen-parallel strike slip displacements in the Precordillera of northern Chile: Geologische Rundschau, v. 80, p. 135–153.

Reutter, K.-J., Scheuber, E., and Chong, G., 1996, The Precordilleran fault system of Chuquicamata, northern Chile: Evidence for reversals along arc-parallel strike-slip faults: Tectonophysics, v. 259, p. 213–228.

Richards, J.P., Boyce, A.J., and Pringle, M.S., 2001, Geologic evolution of the Escondida area, northern Chile: A model for spatial and temporal localization of porphyry Cu mineralization: Economic Geology, v. 96, p. 271–305.

Ridolfi, F., and Renzulli, A., 2012, Calcic amphiboles in calc-alkaline and alkaline magmas: Thermobarometric and chemometric empirical equations valid up to 1,130°C and 2.2 GPa: Contributions to Mineralogy and Petrology, v. 163, p. 877–895.

Ridolfi, F., Renzulli, A., and Puerini, M., 2010, Stability and chemical equilibrium of amphibole in calc-alkaline magmas: An overview, new thermobarometric formulations and application to subduction-related volcanoes: Contributions to Mineralogy and Petrology, v. 160, p. 45–66.

Riquelme, R., Tapia, M., Campos, E., Mpodozis, C., Carretier, S., González, R., Muñoz, S., Fernández-Mort, A., Sanchez, C., and Marquardt, C., 2017, Supergene and exotic Cu mineralization occur during periods of landscape stability in the Centinela mining district, Atacama Desert: Basin Research, v. 30, p. 395–425.

Rivera, S.L., Alcota, H., Fontecilla, C., and Kovacic, P., 2009, Supergene modification of porphyry columns and the application to exploration with special reference to the southern part of the Chuquicamata district, Chile: Society of Economic Geologists, Special Publication 14, p. 1–14.

Rogers, G., and Hawkesworth, C.J., 1989, A geochemical traverse across the North Chilean Andes: Evidence for crust generation from the mantle wedge: Earth and Planetary Science Letters, v. 91, p. 271–285.

Rowland, M.G., and Clark, A.H., 2001, Temporal overlap of supergene alteration and high-sulfidation mineralization in the Spence porphyry copper deposit, II region, Chile [abs.]: Geological Society of America Abstracts with Programs, v. 33, p. A-358.

Rutherford, M.J., and Hill, P.M., 1993, Magma ascent rates from amphibole breakdown: An experimental study applied to the 1980–1986 Mount St. Helens eruptions: Journal of Geophysical Research: Solid Earth, v. 98, p. 19,667–19,685.

Sanchez, C., Brichau, S., Riquelme, R., Carretier, S., Bissig, T., Lopez, C., Mpodozis, C., Campos, E., Regard, V., Hérail, G., and Marquardt, C., 2018, Exhumation history and timing of supergene copper mineralisation in an arid climate: New thermochronological data from the Centinela district, Atacama, Chile: Terra Nova, v. 30, p. 78–85.

Schaltegger, U., Schmitt, A.K., and Horstwood, M.S.A., 2015, U-Th-Pb zircon geochronology by ID-TIMS, SIMS, and laser ablation ICP-MS: Recipes, interpretations, and opportunities: Chemical Geology, v. 402, p. 89–110.

Scheuber, E., Bogdanic, T., Jensen, A., and Reutter, K.-J., 1994, Tectonic development of the north Chilean Andes in relation to plate convergence and magmatism since the Jurassic, *in* Reutter, K.-J., Scheuber, E., and Wigger, P.J., eds., Tectonics of the southern Central Andes: Berlin/Heidelberg, Springer Verlag, p. 121–139.

Schmidt, M.W., 1992, Amphibole composition in tonalite as a function of pressure: An experimental calibration of the Al-in-hornblende barometer: Contributions to Mineralogy and Petrology, v. 110, p. 304–310.

Seedorff, E., Dilles, J.H., Proffett, J.M., Einaudi, M.T., Zurcher, L., Stavast, W.J.A., Johnson, D.A., and Barton, M.D., 2005, Porphyry deposits: Characteristics and origin of hypogene features: Economic Geology 100th Anniversary Volume, p. 251–298.

Sellés, D., Gardeweg, M., and Garibaldi, N., 2016, Geología del área Pampa Lirima-Cancosa, Región de Tarapacá: Servicio Nacional de Geología y Minería, Carta Geológica de Chile, Serie Geología Básica, no. 182, 1 map, scale 1:100,000.

SERNAGEOMIN, 2003, Carta geologica de Chile: Servicio Nacional de Geología y Minería, scale 1:1,000,000.

Sillitoe, R.H., 1994, Erosion and collapse of volcanoes: causes of telescoping in intrusion-centered ore deposits: Geology, v. 22, p. 945–948.

——1998, Major regional factors favouring large size, high hypogene grade, elevated gold content and supergene oxidation and enrichment of porphyry copper deposits, *in* Porter, T.M., ed., Porphyry and hydrothermal copper and gold deposits: A global perspective: Adelaide, PGC Publishing, p. 21–31.

——1999, Styles of high-sulphidation gold, silver and copper mineralisation in porphyry and epithermal environments: Australasian Institute of Mining and Metallurgy, Pacrim '99 Congress, Bali, Indonesia, 1999, Proceedings, p. 29–44.

——2000, Gold-rich porphyry deposits: Reviews in Economic Geology, v. 13, p. 315–345.

——2005, Supergene oxidized and enriched porphyry copper and related deposits: Economic Geology 100th Anniversary Volume, p. 723–768.

——2010, Porphyry copper systems: Economic Geology, v. 105, p. 3–41.

Sillitoe, R.H., and McKee, E.H., 1996, Age of supergene oxidation and enrichment in the Chilean porphyry copper province: Economic Geology, v. 91, p. 164–179.

Sillitoe, R.H., and Perelló, J., 2005, Andean copper province: Tectonomagmatic settings, deposit types, metallogeny, exploration, and discovery: Economic Geology 100th Anniversary Volume, p. 845–890.

Sillitoe, R.H., Marquardt, J.C., Ramirez, F., Becerra, H., and Gómez, M., 1998, Geology of the concealed MM porphyry copper deposit,

Chuquicamata district, northern Chile: Society of Economic Geologists, Special Publication 5, p. 59–69.
Sillitoe, R.H., Devine, F.A.M., Sanguinetti, M.I., and Friedman, R.M., 2019, Geology of the Josemaría porphyry copper-gold deposit, Argentina: Formation, exhumation, and burial in two million years: Economic Geology, v. 114, p. 407–425.
Singer, D.A., Berger, V.I., and Moring, B.C., 2008, Porphyry copper deposits of the world: Database and grade and tonnage models: U.S. Geological Survey, Open-File Report 2008-1155, 45 p.
Skarmeta, J., 1983, The structural geology of the Sierra de Moreno, northern Chile: Unpublished Ph.D. thesis, London, United Kingdom, University of London, 299 p.
Stalder, N.F., Herman, F., Fellin, G.M., Coutand, I., Aguilar, G., Reiners, P.W., and Fox, M., 2020, The relationships between tectonics, climate and exhumation in the Central Andes (18–36°S): Evidence from low-temperature thermochronology: Earth-Science Reviews, v. 8, p. 1–37.
Thiede, R.C., and Ehlers, T.A., 2013, Large spatial and temporal variations in Himalayan denudation: Earth and Planetary Science Letters, v. 371–372, p. 278–293.
Thomas, W.M., and Ernst, W.G., 1990, The aluminum content of hornblende in calc-alkaline granitic rocks: A mineralogic barometer calibrated experimentally to 12 kbars: Geochemical Society, Special Publication 2, p. 59–63.
Tomlinson, A.J., and Blanco, N., 2008, Geología de la franja El Abra-Chuquicamata, II Región (21°45'-22°30'S): Servicio Nacional de Geología y Minería, Informe Registrado IR-08-35, 196 p.
Tomlinson, A.J., Blanco, N., Maksaev, V., Dilles, J.H., Grunder, A.L., and Ladino, M., 2001, Geología de la Precordillera Andina de Quebrada Blanca-Chuquicamata, Regiones I y II (20°30′-22°30′S): Servicio Nacional de Geología y Minería, Informe Registrado IR-01-20, 444 p.
Tomlinson, A.J., Blanco, N., García, M., Baeza, L., Alcota, H., Ladino, M., De, C.P., Fanning, C.M., and Martin, M.W., 2012, Permian exhumation of metamorphic complexes in the Calama area: Evidence for flat-slab subduction in northern Chile during the San Rafael tectonic phase and origin of the Central Andean gravity high [ext. abs.]: Congreso Geológico Chileno, 13th, Antofagasta, Chile, 2012, Proceedings, p. 209–211.
Tomlinson, A.J., Blanco, N., and Ladino, M., 2015, Carta Mamiña, Región de Tarapacá: Servicio Nacional de Geología y Minería, Carta Geológica de Chile, Serie Geología Básica 174, 1 map, scale 1:100,000.
van Zalinge, M.E., Sparks, R.S.J., Cooper, F.J., and Condon, D.J., 2016, Early Miocene large-volume ignimbrites of the Oxaya Formation, Central Andes: Journal of the Geological Society, London, v. 173, p. 716–733.
van Zalinge, M.E., Sparks, R.S.J., Evenstar, L.A., Cooper, F.J., Aslin, J., and Condon, D.J., 2017, Using ignimbrites to quantify structural relief growth and understand deformation processes: Implications for the development of the Western Andean slope, northernmost Chile: Lithosphere, v. 9, p. 29–45.
Vasconcelos, P.M., 1999, K-Ar and $^{40}Ar/^{39}Ar$ Geochronology of weathering processes: Annual Review of Earth and Planetary Sciences, v. 27, p. 183–229.
Vergara, H., and Thomas, A., 1984, Hoja Collacagua, Región de Tarapacá: Servicio Nacional de Geología y Minería, Carta Geológica de Chile, no. 59, 1 map, scale 1:250,000.
Vicente, J.-C., 2006, Dynamic paleogeography of the Jurassic Andean basin: Pattern of regression and general considerations on main features: Revista de la Asociación Geológica Argentina, v. 61, p. 408–437.
Wendt, I., and Carl, C., 1991, The statistical distribution of the mean squared weighted deviation: Chemical Geology: Isotope Geoscience Section, v. 86, p. 275–285.
Wilkinson, B.H., and Kesler, S.E., 2007, Tectonism and exhumation in convergent margin orogens: Insights from ore deposits: The Journal of Geology, v. 115, p. 611–627.
Wörner, G., Hammerschmidt, K., Henjes-Kunst, F., Lezaun, J., and Wilke, H., 2000, Geochronology ($^{40}Ar/^{39}Ar$, K-Ar and He-exposure ages) of Cenozoic magmatic rocks from Northern Chile (18–22°S): Implications for magmatism and tectonic evolution of the central Andes: Revista Geologica De Chile, v. 27, p. 205–240.
Yanites, B.J., and Kesler, S.E., 2015, A climate signal in exhumation patterns revealed by porphyry copper deposits: Nature Geoscience, v. 8, p. 462–465.
Zentilli, M., Maksaev, V., Boric, R., and Wilson, J., 2018, Spatial coincidence and similar geochemistry of Late Triassic and Eocene-Oligocene magmatism in the Andes of northern Chile: Evidence from the MMH porphyry type Cu-Mo deposit, Chuquicamata district: International Journal of Earth Sciences, v. 107, p. 1097–1126.

Simon Dahlström received his Ph.D. degree in earth sciences from the University of Bristol, United Kingdom, in 2020. His Ph.D. project was fully funded by BHP and investigated how granite emplacement and exhumation in the Central Andes can be tied to porphyry copper deposit formation, enrichment, and preservation. Before moving to Bristol, he obtained his M.Sc. degree at Åbo Akademi University in Turku, Finland, and worked on exploration projects for several companies in northern Sweden and Finland. Simon currently works as a project geologist at Terrafame Ltd. in Sotkamo, Finland, investigating the Paleoproterozoic Kolmisoppi Ni-Zn-Cu-Co deposit.